Chapter 13
Radio Resource Management

When a new call arrives, mobile station (MS) must be connected to a suitable base station (BS) or perhaps a set of BSs. Also, as a MS traverses from one cell to the next handoffs are required so that an acceptable link quality can be maintained; otherwise the required increase in transmit power to compensate for path loss will result in excessive co-channel and adjacent channel interference. The failure to handoff a MS as it moves from one cell to the next will also tend to increase the call blocking probability, because some cells may carry more traffic than planned. For TDMA cellular systems that do not employ frequency hopping, an intra-cell handoff is sometimes desirable when the link with the serving BS is affected by excessive interference, while another link with the same BS can provide better quality. The handoff mechanism consists of two processes: (1) link quality evaluation and handoff initiation, (2) allocation of radio and network resources.

In general, cellular systems with smaller cell sizes require faster and more reliable link quality evaluation and handoff algorithms. Labedz [190] has shown that the number of cell boundary crossings is inversely proportional to the cell size. Furthermore, Nanda [239] has shown that the handoff rate increases with only the square root of the call density in macrocells, but it increases linearly with the call density in microcells. Since the MS has a certain probability of handoff failure each time a handoff is attempted, it is clear that handoff algorithms must become more robust and reliable as the cell sizes decrease.

One of the major tasks in a cellular system is to monitor the link quality and determine when handoff is required. If a handoff algorithm does not detect poor signal quality fast enough, or makes too many handoffs, then capacity is diminished due to increased co-channel interference and/or excessive control traffic. A variety of parameters such as bit error rate (BER) [77], carrier-to-interference ratio, C/I [126], distance [112, 223], traffic load, signal strength [62, 149, 150, 223, 233, 331], and various combinations of these fundamental schemes have been suggested for evaluating the link quality and deciding when a handoff should be performed. One possibility is to measure the received carrier plus interference power, $C + I$. However, a large $C + I$ does not necessary imply a large C/I. Since the radio link quality depends more on the C/I than the $C + I$, it is apparent that C/I based handoff algorithms are necessary for high capacity cellular systems. A discussion of C/I measurement techniques is included in this chapter.

Based on the roles that the BSs and MSs perform in the process of link quality evaluation and handoff initiation, there are three categories of handoff algorithms. The first is a network-controlled handoff (NCHO) algorithm, which was used in first generation cellular systems. With a NCHO algorithm, the reverse link quality is monitored by the serving BS and the surrounding BSs, typically using measurements of the received $C+I$. The reverse link $C+I$ measurements are forwarded to a mobile switching center (MSC), which ultimately makes the handoff decision. Typically, these centralized NCHO algorithms only supported inter-cell handoffs, had handoff delays on the order of several seconds, and relied on relatively infrequent measurements and reports of the reverse link $C + I$ values.

The second type of handoff algorithm is the mobile-assisted handoff (MAHO) algorithm which is widely used in modern cellular systems. MAHO algorithms use both the serving BS and the MS to measure the reverse and forward link quality, respectively, usually based on the received C/I. However, link quality measurements of the alternate BSs are only obtained by the MS. The MS periodically relays the link quality measurements of the serving and alternate BSs back to the serving BS, and the handoff decision is still made by the serving BS along with the MSC. MAHO algorithms typically support both intra-cell and inter-cell handoffs. MAHO algorithms typically use frequent updates of the link quality measurements, and have much lower handoff delays than a NCHO algorithm.

The third type of handoff algorithm is the decentralized mobile-controlled handoff (MCHO) algorithm. With MCHO algorithms, the link quality with the serving BS is measured by both the serving BS and the MS. Like a MAHO algorithm, the measurements of link quality for alternate BSs are done at the MS, and both intra-cell and inter-cell handoffs are supported. However, unlike the MAHO algorithms, the link measurements at the serving BS are relayed to the MS, and the handoff

G.L. Stüber, *Principles of Mobile Communication*, DOI 10.1007/978-3-319-55615-4_13

decision is made by the MS. MCHO algorithms typically have the lowest handoff network delays and are the most reliable. However, since the handoff decisions are made by the MS, network-wide radio resource optimization is more difficult. MCHO algorithms are typically used with cordless telephone systems.

Handoff algorithms can be categorized into forward and backward types depending on how the handoff process is initiated. Backward handoff algorithms initiate the handoff process through the serving BS, and no access to the "new" channel is made until the control entity of the new channel has confirmed the allocation of resources. The advantage of backward algorithms is that the signaling information is transmitted through an existing radio link and, therefore, the establishment of a new signaling channel is not required during the initial stages of the handoff process. The disadvantage is that the algorithm may fail in conditions where the link quality with the serving BS is rapidly deteriorating. This type of handoff is widely used in TDMA cellular systems such as GSM. Forward handoff algorithms initiate the handoff process via a channel with the target BS without relying on the "old" channel during the initial phase of the handoff process. The advantage is a faster handoff process, but the disadvantage is a reduction in handoff reliability. Finally, handoffs can also be categorized as hard handoffs and soft handoffs.

With hard handoffs, a MS can connect to only one BS at a time. An absolute (binary) decision is made to initiate and execute a handoff without making a number of simultaneous connections among candidate BSs. The handoff is initiated based on a hysteresis imposed on the current link. The target BS is already selected prior to executing the handoff based on link measurements and the active connection is transferred to the target BS instantly. The connection experiences a brief interruption during the actual transfer because the MS can only connect to one BS at a time. Hard handoffs do not take advantage of the diversity gain opportunity during handoff, where the signals from two or more BSs arrive at comparable strengths. Yet, it is a simple and inexpensive way to implement handoff. This type of handoff is used in TDMA cellular systems such as GSM.

Hard handoff algorithms have been optimized by minimizing two conflicting design criteria: the handoff delay and the mean number of handoffs between BSs. It is important to keep the handoff delay small to prevent dropped calls and to prevent an increase in co-channel interference due to distortion of the cell boundaries. Likewise, it is important to keep the mean number of handoffs between BSs along a handoff route at a reasonably low value to prevent excessive control signaling and resource consumption on the network. Several authors [150, 223, 233, 331] have applied these (or similar) design criteria while adjusting two important design parameters: the required average signal strength difference, or hysteresis H, between the BSs before a hard handoff is initiated, and the temporal window length T over which the signal strength measurements are averaged. The handoff hysteresis prevents excessive handoffs due to "ping-ponging" between BSs. The best choice of T and H depends on the propagation environment. Usually, the averaging interval T is chosen to correspond to a spatial distance of 20–40 carrier wavelengths, and the hysteresis H is chosen on the order of the shadow standard deviation.

Murase [233] studied the tradeoff between the hysteresis and window length for line-of-sight (LoS) and non-line-of-sight (NLoS) hard handoffs. For LoS handoffs, the MS always maintains a LoS with both the serving and target BS. NLoS handoffs, on the other hand, arise when the MS suddenly loses the LoS component with the serving BS while gaining a LoS component with the target BS. This phenomenon is sometimes called the "corner effect" [62, 233] since it occurs while turning corners in urban microcellular settings like the one shown in Fig. 13.1, where the MS traverses along a route from BS_0 to BS_1. In this case, the average received signal strength with the serving BS can drop by 25–30 dB over distance as small as 10 m [233].

Corner effects may also cause link quality imbalances on the forward and reverse channels due to the following mechanism. Quite often the co-channel interference will arrive via a NLoS propagation path. Hence, as a MS rounds a corner, the received signal strength at the serving BS suffers a large decrease while the NLoS co-channel interference remains the same, i.e., the corner effect severely degrades the C/I on the reverse channel. Meanwhile, the corner will cause the same

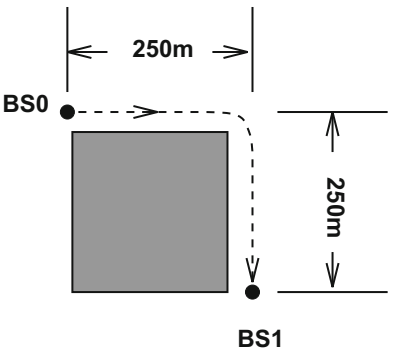

Fig. 13.1 Typical NLoS handoff scenario. The MS rounds the corner, losing the LoS from BS_0, and gaining the LoS from BS_1

attenuation to both the desired and interfering signals that are received at the MS. Therefore, unless there are other sources of co-channel interference that become predominant as the MS rounds the corner, the C/I on the forward channel will remain about the same.

If the handoff requests from rapidly moving MSs in microcellular networks are not processed quickly, then excessive dropped calls will occur. Fast temporal based hard handoff algorithms can partially solve this problem, where short temporal averaging windows are used to detect large, sudden, drops in signal strength [233]. However, the shortness of a temporal window is relative to the MS velocity and, furthermore, a fixed time averaging interval makes the hard handoff performance sensitive to velocity with the best performance being achieved at only a particular velocity. Velocity adaptive handoff algorithms can overcome this problem, and are known to be robust to the severe propagation environments that are typical of urban microcellular networks [28].

With soft handoffs, a MS can connect to a number of candidate BSs during a handoff process. Eventually, the handoff is completed when the MS selects the best candidate BS as the target. Soft handoff is more careful in selecting the target BS, because the target BS needs to be the best candidate from among the available BSs. During the handoff process, soft handoff further enhances the system performance through diversity reception. Unlike hard handoff, the necessary link quality measurements for handoff are done by the MS, where it constantly monitors the signals from surrounding BSs. Soft handoff is a type of MAHO. However, all these advantages do not imply that soft handoff is without its weaknesses. Soft handoff is complex and expensive to implement. Also, forward link interference actually increases with soft handoff since several BSs, instead of one, can connect to the same MS. This increase in forward link interference can become a problem if the handoff region is large, such that there are many MSs in soft handoff mode.

Soft handoff has a special importance in CDMA based systems, due to its close relationship with power control. CDMA systems are interference-limited meaning their capacities are closely related to the amount of interference the systems can tolerate. Due to universal frequency reuse, a CDMA system cell is affected by not only interference within its own cell, but also interference from its neighboring cells. To alleviate the level of interference, and thus increase the capacity and quality, CDMA systems employ power control. Power control attempts to solve the near/far problem by adjusting transmit power so that the target C/I is evenly satisfied. The fundamental idea behind power control is to restrain mobile stations (MSs) and base stations (BSs) from transmitting more power than is necessary in order to limit excess interference. With power control, each MS (or BS) is disciplined to transmit just enough power to meet the target C/I level. However, in order for power control to work properly, the system must ensure that each MS is connected to the BS having the least path attenuation at all times; otherwise, a positive feedback problem can destabilize the entire system. Soft handoff ensures that each MS is served by the best BS a majority of the time, by allowing connections to multiple BSs with macroscopic selection diversity.

To illustrate the necessity for soft handoff in CDMA cellular systems, consider a simple system consisting of two BSs and two MSs as shown in Fig. 13.2. Let us assume that each MS must satisfy a target $C/I = 1$. Let C_{11}, C_{12}, C_{21}, and C_{22} be equal to 5, 6, 7, and 4, respectively. With soft handoff, each MS connects to the best available BS; MS_1 connects to BS_2 and MS_2 connects to BS_1. Then $(C/I)_1 = C_{12}/C_{22} = 6/4$ and $(C/I)_2 = C_{21}/C_{11} = 7/5$, and $(C/I)_1$ and $(C/I)_2$ both satisfy the target C/I. However without soft handoff, the system can no longer guarantee that the MSs are connected to the best BSs. Assume that MS_1 is connected to BS_1 and MS_2 is connected to BS_2. Then, $(C/I)_1 = C_{11}/C_{21} = 5/7$ and $(C/I)_2 = C_{22}/C_{12} = 4/6$. Since both $(C/I)_1$ and $(C/I)_2$ fail to meet the target C/I, power control will attempt to increase the C/I's by increasing the MS transmit powers. But for the given setting, increasing the MS transmit powers also increases

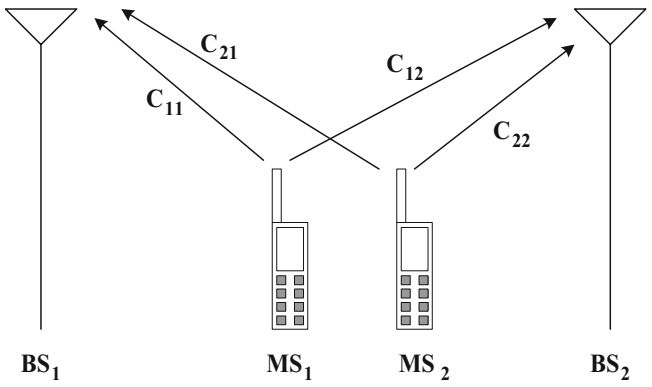

Fig. 13.2 Soft handoff example, from [274]

the respective interference levels and the C/I's continue to stay below the target C/I, causing a positive power feedback effect. Soft handoff does indeed ensure that each MS is served by the best BS a majority of the time. For this reason it is a *required* feature in CDMA cellular systems.

Although the best handoff algorithm is the one that maximizes the capacity of the network, there are many criterion to judge the performance of a handoff algorithm. These include the probability of handoff initiation, probability of dropped call, the mean number of handoff requests as a MS traverses over a handoff route, and the delay before a handoff is initiated after a MS crosses an established cell boundary. These quantities depend on the measure of link quality and the propagation environment. Finally, network parameters such as the probabilities of new call blocking, the probability of forced termination, and handoff queuing time are important. Moreover, it may be desirable to distinguish between dropped calls that are due to a failed handoff mechanism, and forced terminations that are due to the lack of an unavailable channel in the target cell after successful initiation of the handoff process.

The remainder of this chapter is organized as follows. Section 13.1 presents several different types of signal strength based handoff algorithms and Sect. 13.2 introduces pilot-to-interference ratio based soft handoff algorithms. This is followed by a detailed treatment of spatial signal strength averaging in Sect. 13.3. Guidelines are developed on the window averaging length that is needed so that Ricean fading can be neglected in analog and sampled averaging. These guidelines are necessary for local mean and velocity estimation. Section 13.4 motivates the need for velocity adaptive handoff algorithms and presents three velocity estimators. The velocity estimators are compared in terms of their sensitivity to Rice factor, directivity, and additive Gaussian noise. In Sect. 13.5, the velocity estimators are incorporated into a velocity adaptive handoff algorithm. Section 13.6 provides an analytical treatment of conventional signal strength based hard handoff algorithms while Sect. 13.7 does the same for soft handoff algorithms. Finally, Sect. 13.8 discusses methods for C/I measurements in TDMA cellular systems.

13.1 Signal Strength Based Hard Handoff Algorithms

Traditional MAHO algorithms use signal strength estimates that are obtained by calculating time averages of the received squared-envelope, $\langle|\tilde{r}_i(t)|^2\rangle$, from N neighboring BSs, BS_i, $i = 0,\ldots,N-1$. A MS is reconnected to an alternate BS whenever the signal strength estimate of the target BS exceeds that of the serving BS by at least a factor of H. For example, a handoff is performed between two BSs, BS_0 and BS_1, when

$$\begin{aligned}\bar{\Omega}_{p,1}(n) &> \bar{\Omega}_{p,0}(n)H \quad \text{if the serving BS is BS}_0\\ \bar{\Omega}_{p,0}(n) &> \bar{\Omega}_{p,1}(n)H \quad \text{if the serving BS is BS}_1,\end{aligned} \tag{13.1}$$

where H denotes the hysteresis, and $\bar{\Omega}_{p,0}(n)$ and $\bar{\Omega}_{p,1}(n)$ are the estimated local mean signal strengths of BS_0 and BS_1, given by

$$\bar{\Omega}_{p,0}(n) = \frac{1}{N}\sum_{k=n-N+1}^{n}|r_0(k)|^2 \tag{13.2}$$

$$\bar{\Omega}_{p,1}(n) = \frac{1}{N}\sum_{k=n-N+1}^{n}|r_1(k)|^2, \tag{13.3}$$

respectively, where $|\tilde{r}_i(kT_s)|^2$ is the kth sample of the received squared-envelope, T_s is the sampling period, and N is the window length.

Many other variations of signal strength based handoff algorithms have been suggested in the literature. In one variation, handoffs are also triggered when the measured signal strength of the serving BS drops below a threshold. For example, a handoff could be performed between BS_0 and BS_1 when

$$\begin{aligned}&\bar{\Omega}_{p,1}(n) > \bar{\Omega}_{p,0}(n)H \text{ and } \bar{\Omega}_{p,0}(n) > \Omega_{\text{L}}, \quad \text{if the serving BS is BS}_0\\ &\bar{\Omega}_{p,1}(n) > \bar{\Omega}_{p,0}(n) \text{ and } \bar{\Omega}_{p,0}(n) < \Omega_{\text{L}}, \quad \text{if the serving BS is BS}_0\end{aligned}$$

$$\begin{aligned}
&\bar{\Omega}_{p,0}(n) > \bar{\Omega}_{p,1}(n)H \text{ and } \bar{\Omega}_{p,1}(n) > \Omega_{\mathrm{L}}, \quad \text{if the serving BS is BS}_1 \\
&\bar{\Omega}_{p,0}(n) > \bar{\Omega}_{p,1}(n) \text{ and } \bar{\Omega}_{p,1}(n) < \Omega_{\mathrm{L}}, \quad \text{if the serving BS is BS}_1.
\end{aligned} \tag{13.4}$$

This scheme encourages a handoff whenever the received signal strength from the serving BS drops below the threshold Ω_{L}, thereby reducing the probability of a dropped call.

Another variation discourages handoffs when the received signal strength from the serving BS exceeds another threshold Ω_{U}. For example, a handoff is performed between BS_0 and BS_1 when

$$\begin{aligned}
&\bar{\Omega}_{p,1}(n) > \bar{\Omega}_{p,0}(n)H \text{ and } \Omega_{\mathrm{L}} < \bar{\Omega}_{p,0}(n) < \Omega_{\mathrm{U}}, \quad \text{if the serving BS is BS}_0 \\
&\bar{\Omega}_{p,1}(n) > \bar{\Omega}_{p,0}(n) \text{ and } \bar{\Omega}_{p,0}(n) < \Omega_{\mathrm{L}}, \quad \text{if the serving BS is BS}_0 \\
&\bar{\Omega}_{p,0}(n) > \bar{\Omega}_{p,1}(n)H \text{ and } \Omega_{\mathrm{L}} < \bar{\Omega}_{p,1}(n) < \Omega_{\mathrm{U}}, \quad \text{if the serving BS is BS}_1 \\
&\bar{\Omega}_{p,0}(n) > \bar{\Omega}_{p,1}(n) \text{ and } \bar{\Omega}_{p,1}(n) < \Omega_{\mathrm{L}}, \quad \text{if the serving BS is BS}_1.
\end{aligned} \tag{13.5}$$

This scheme avoids unnecessary handoffs, thereby reducing the network signaling load and network delay.

Direction biased handoff algorithms have also been suggested for improving the handoff performance in urban microcells [26]. These algorithms incorporate moving direction information into the handoff algorithm to encourage handoffs to BSs that the MS is approaching, and to discourage handoffs to BSs that the MS is moving away from. Let BS_{s} denote the serving BS. A direction biased handoff algorithm can be defined by grouping all the BSs being considered as handoff candidates, including the serving base station BS_{s}, into two sets based on their direction information. Define the following sets:

$$\mathscr{A} := \text{the set of BSs the MS is approaching} \tag{13.6}$$

$$\mathscr{R} := \text{the set of BSs the MS is moving away from.} \tag{13.7}$$

By introducing an encouraging hysteresis H_{e}, and a discouraging hysteresis H_{d}, a direction biased handoff algorithm requests a handoff to BS_j if $\mathrm{BS}_j \in \mathscr{R}$ and

$$\begin{aligned}
&\bar{\Omega}_{p,j}(n) > \bar{\Omega}_{p,s}(n)H, \quad \text{if } \mathrm{BS}_{\mathrm{s}} \in \mathscr{R} \\
&\bar{\Omega}_{p,j}(n) > \bar{\Omega}_{p,s}(n)H_{\mathrm{d}}, \quad \text{if } \mathrm{BS}_{\mathrm{s}} \in \mathscr{A}
\end{aligned} \tag{13.8}$$

or if $\mathrm{BS}_j \in \mathscr{A}$ and

$$\begin{aligned}
&\bar{\Omega}_{p,j}(n) > \bar{\Omega}_{p,s}(n)H_e, \quad \text{if } \mathrm{BS}_{\mathrm{s}} \in \mathscr{R} \\
&\bar{\Omega}_{p,j}(n) > \bar{\Omega}_{p,s}(n)H, \quad \text{if } \mathrm{BS}_{\mathrm{s}} \in \mathscr{A}.
\end{aligned} \tag{13.9}$$

To encourage handoffs to BSs in $\mathscr{A}$ and discourage handoffs to BSs in $\mathscr{R}$, the hysteresis values should satisfy $H_{\mathrm{e}} \leq H \leq H_{\mathrm{d}}$. When equality holds, the algorithm reduces to the conventional method described in (13.1). Good values for H_{e}, H, and H_{d} depend on the propagation environment and BS layout. In general, a direction biased handoff algorithm can maintain a lower mean number of handoffs and handoff delay, and provide better cell membership properties.

13.2 Pilot-to-Interference Ratio Based Soft Handoff Algorithms

In CDMA based systems each BS transmits a pilot signal to assist soft handoff [105]. In synchronous CDMA systems such as cdma2000, all BSs use the same pilot sequence and the BSs are distinguished by using different phase shifts of the same sequence. In asynchronous CDMA systems such as WCDMA, each cell is allocated a distinct pilot sequence. In any case, the MSs use the pilot signals to initiate and complete handoffs. Each pilot signal is used to measure the pilot-to-interference ratio (PIR), which is the ratio of received pilot energy per chip to total interference spectral density:

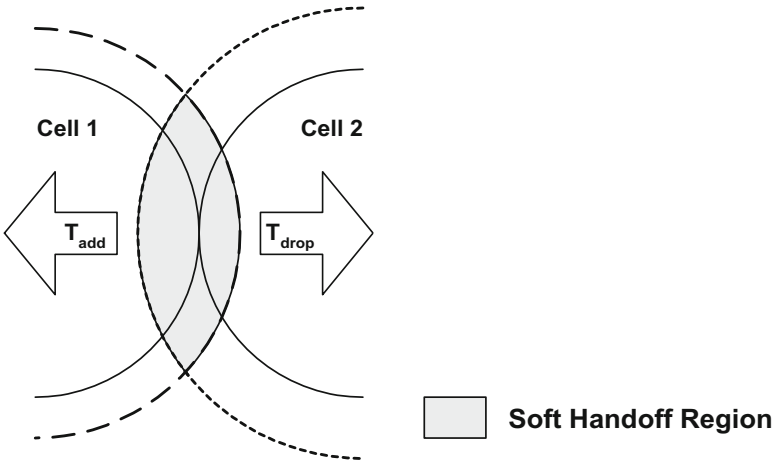

Fig. 13.3 Soft handoff boundaries and region

$$\text{PIR} = \frac{E_c}{I_o}. \tag{13.10}$$

An *active set* refers to the set of BSs to which a MS is connected at any given time. The active set contains a single BS most of time, but additional BSs are added to the active set during soft handoff.

Soft handoffs are initiated based on a hysteresis imposed on the PIRs. An upper threshold, T_{add}, determines the pilot signal level for which qualifying BSs are added to the active set, whereas a lower threshold, T_{drop}, determines when the weak pilot BSs are dropped from the active set. The handoff margin, the difference between T_{add} and T_{drop}, is an indicator of how long a soft handoff will take on average. A wider margin results in a longer average soft handoff duration. Figure 13.3 shows how changes in the handoff parameters affect the handoff region. Reducing T_{drop} and T_{add} expands the cell boundaries and thus increases the soft handoff region.

The soft handoff margin and thresholds are very important parameters in determining system performance, and need to be carefully optimized for a given situation. Allowing more MSs to be in soft handoff mode will decrease the reverse link interference, by allowing more MSs to benefit from macrodiversity. That is, the MSs in handoff are connected to the best available link and, therefore, do not transmit excessive power. However, the increase in the number of MSs in soft handoff and the increase in the average handoff duration can increase system complexity and tie up already scarce system resources. Also, as mentioned previously, soft handoff increases the forward link interference by allowing multiple BSs to transmit to one MS. The challenge is to optimized the handoff parameters so that the capacity and quality of service requirements are satisfied, while keeping the operational cost and system complexity down. Other important soft handoff parameters include the T_{drop} timer and the ratio between the handoff region and total cell area. The T_{drop} timer is the length of time that a signal level must remain below T_{drop} to drop a BS from the active set.

13.3 Signal Strength Averaging

The received squared-envelopes $|\tilde{r}(t)|^2$ are affected by Ricean fading, log-normal shadowing, and path loss attenuation. Here, the two Ricean fading models discussed in Sect. 2.1.3.2 are considered. The first model assumes that the quadrature components of the complex fading envelope $g(t) = g_I(t) + jg_Q(t)$ are independent Gaussian random processes with variance b_0 and means $m_I(t) = m_I$ and $m_Q(t) = m_Q$, respectively. In this case, the envelope $\alpha(t) = |g(t)|$ is Ricean distributed with Rice factor $K = s^2/(2b_0)$, where $s^2 = m_I^2 + m_Q^2$. The second model is more realistic and uses the time-varying means $m_I(t)$ and $m_Q(t)$ in (2.59) and (2.60), respectively. Once again, the envelope $\alpha(t)$ is Ricean distributed with Rice factor $K = s^2/(2b_0)$. Both models are equivalent for Rayleigh fading ($K = 0$). As suggested in Sect. 2.6.1, shadow correlation can be described by the model in (2.6.1). Finally, for LoS propagation, the two-slope path loss model in (2.410) is assumed. For NLoS propagation, the model in (2.412) is assumed yielding, for example, the received signal strength profile in Fig. 2.67.

13.3.1 Choosing the Proper Window Length

When a time average of the received complex squared-envelope $\langle|\tilde{r}_i(t)|^2\rangle$ is calculated, an averaging interval or temporal window length must be chosen. One method for determining the proper window length is to use analog averaging. The following development extends the original work of Lee [199] by incorporating Aulin's Ricean fading model. With Lee's multiplicative model, the squared-envelope of the composite signal at position y is

$$\hat{\alpha}_c^2(y)^2 = \alpha^2(y) \cdot \Omega_p(y) \tag{13.11}$$

where $\alpha^2(y)$ is a non-central chi-square random variable with 2 degrees of freedom (Ricean fading), and $\Omega_p(y)$ is a log-normal random variable (log-normal shadowing). Since the local mean remains constant over short spatial distances, it is assumed that $\Omega_p(y) = \Omega_p$ over the spatial averaging interval. However, if the spatial averaging interval is too large, this assumption will no longer be valid since the time-average $\langle|\tilde{r}_i(t)|^2\rangle$ will average over the shadowing process as well. Assuming that the envelope fading is an ergodic random process, an integral spatial average of $\hat{\alpha}_c^2(y)$ can be used to estimate the local mean Ω_p, i.e.,

$$\bar{\Omega}_p = \frac{1}{2L}\int_{x-L}^{x+L} \hat{\alpha}_c^2(y)dy \;=\; \frac{\Omega_p}{2L}\int_{x-L}^{x+L} \alpha^2(y)\mathrm{d}y, \tag{13.12}$$

where the second equality holds since $\Omega_p(y)$ is constant over the spatial interval $(x-L, x+L)$. The accuracy of the estimate can be determined from the variance of (13.12), calculated as [195]

$$\sigma^2_{\bar{\Omega}_p} = \frac{1}{L}\int_0^{2L}\left(1-\frac{\ell}{2L}\right)\lambda_{\alpha^2\alpha^2}(\ell)\mathrm{d}\ell, \tag{13.13}$$

where $\lambda_{\alpha^2\alpha^2}(\ell) = \mathrm{E}[\alpha^2(y)\alpha^2(y+\ell)] - \mathrm{E}[\alpha^2(y)]\mathrm{E}[\alpha^2(y+\ell)]$ is the *spatial* autocovariance of the squared-envelope, and $\mathrm{E}[\,x\,]$ denotes the ensemble average of x. The spatial autocovariance of the received squared-envelope at a MS with 2-D isotropic scattering can be obtained from (2.94) along with the time-distance transformation $f_m\tau = \ell/\lambda_c$. Substituting (2.94) into (13.13) and using $f_m\tau = \ell/\lambda_c$ yields

$$\sigma^2_{\bar{\Omega}_p} = \left(\frac{\Omega_p}{K+1}\right)^2 \frac{1}{L}\int_0^{2L}\left(1-\frac{\ell}{2L}\right)J_0(2\pi\ell/\lambda_c)\Big(J_0(2\pi\ell/\lambda_c) + 2K\cos\left(2\pi\ell\cos(\theta_0)/\lambda_c\right)\Big)\mathrm{d}\ell. \tag{13.14}$$

As desired, $\sigma^2_{\bar{\Omega}_p} \to 0$ as $L \to \infty$. When L is large, $\bar{\Omega}_p$ can be considered Gaussian since it is the summation of many independent random variables. However, if $\sigma^2_{\bar{\Omega}_p}$ is relatively large compared to Ω_p (due to small L or small Ω_p), then it is more appropriate to treat $\bar{\Omega}_p$ as a non-central chi-square random variable. In this case, it may be more appropriate to approximate $\bar{\Omega}_p$ as a log-normal random variable which has the same general shape as a non-central chi-square distribution (i.e., zero at the origin with an infinitely long tail) [143, 144].

Proceeding under the assumption that $\bar{\Omega}_p$ is approximately Gaussian, the 1σ spread can be calculated to measure the accuracy of the estimator, where

$$1\sigma \text{ spread } = 10\log_{10}\left\{\frac{\Omega_p + \sigma_{\bar{\Omega}_p}}{\Omega_p - \sigma_{\bar{\Omega}_p}}\right\} \tag{13.15}$$

with the interpretation that $\mathrm{P}[|\bar{\Omega}_{p\ (\mathrm{dB})} - \Omega_{p\ (\mathrm{dB})}| \le 1\ \sigma \text{ spread}] = 0.68$.[1] Observe from (13.14) and (13.15) that the accuracy of the local mean estimate depends on K, L, and θ_0. Figure 13.4 shows the 1σ spread when $\theta_0 = 60°$ for various values of K. In general, $\bar{\Omega}_p$ approaches Ω_p with increasing K. However, the angle θ_0 also affects the accuracy as shown in Fig. 13.5. When $\theta_0 = 90°$ the 1 σ spread is minimized, resulting in the best estimate of the local mean. Conversely, the worst estimates

[1] The probability of lying within one standard deviation of the mean of a Gaussian random variable is 0.68.

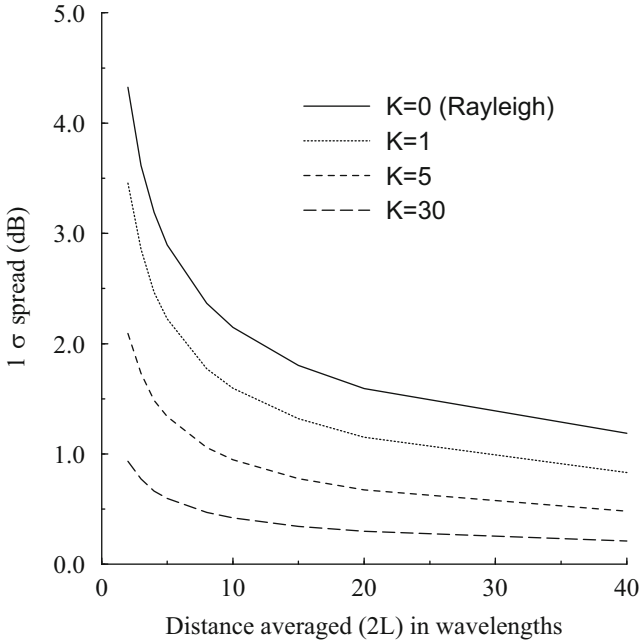

Fig. 13.4 Dependency of the 1σ spread for squared-envelope samples on the averaging distance ($2L$) and Rice factor K when $\theta_0 = 60°$, from [28]

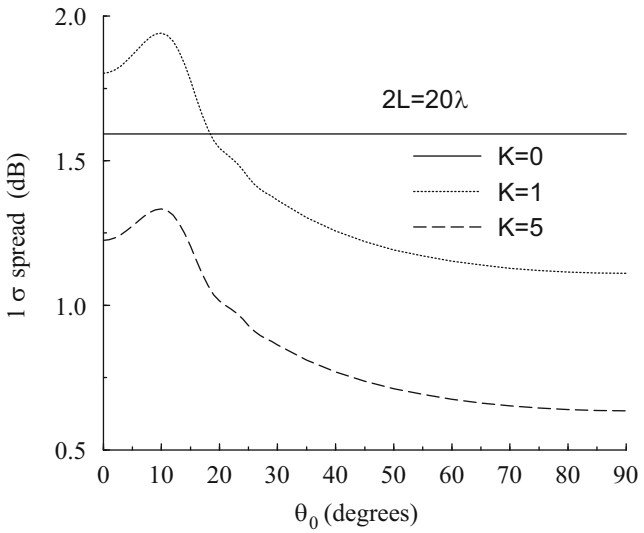

Fig. 13.5 Dependency of the 1σ spread on the specular angle θ_0 mod 90°, from [28]

occur for small θ_0 (in the neighborhood of 10° in Fig. 13.5). The actual angle that the maximum occurs is a function of L, and it can easily be shown that the 1 σ spread has a local minimum at $\theta_0 = 0°$ and global minimum at $\theta_0 = 90°$ for all L. In any case, the required spatial averaging distance for local mean estimation depends on K and θ_0.

13.3.2 Choosing the Proper Number of Samples to Average

Most practical signal strength estimators use samples of the signal strength rather than analog averaging. The number and spacing of samples to provide a good estimate of the local mean must be determined. Consider the sampled composite squared-envelope

$$\alpha_c^2[i] \triangleq \alpha_c^2(iS) \tag{13.16}$$

where S is the spatial sampling period, and i is an integer. Then the spatial average

$$\bar{\Omega}_p = \frac{1}{N}\sum_{i=0}^{N-1}\alpha_c^2[i] \tag{13.17}$$

can be used to determine an unbiased estimate of the local mean Ω_p. As with analog averaging, the variance of this estimate can be used to measure its accuracy, where

$$\sigma^2_{\bar{\Omega}_p} = \frac{1}{N^2}\sum_{i=0}^{N-1}\sum_{j=0}^{N-1}\mathrm{E}\left[\alpha_c^2[i]\alpha_c^2[j]\right] - \left(\mathrm{E}\left[\bar{\Omega}_p\right]\right)^2. \tag{13.18}$$

By using (2.94), the transformation $f_m\tau = \ell/\lambda_c$, and the symmetric properties of the autocovariance function, (13.18) becomes

$$\begin{aligned}\sigma^2_{\bar{\Omega}_p} &= \frac{\lambda_{\alpha^2\alpha^2}(0)}{N} + 2\sum_{j=1}^{N-1}\left(\frac{N-j}{N^2}\right)\lambda_{\alpha^2\alpha^2}(Sj)\\ &= \left(\frac{\Omega_p}{K+1}\right)^2\left(\frac{1+2K}{N} + 2\sum_{j=1}^{N-1}\left(\frac{N-j}{N^2}\right)J_0(2\pi Sj/\lambda_c)\Big(J_0(2\pi Sj/\lambda_c) + 2K\cos\left(2\pi Sj\cos(\theta_0)/\lambda_c\right)\Big)\right),\end{aligned} \tag{13.19}$$

where S is measured in wavelengths (λ_c). Note that $\sigma_{\bar{\Omega}_p}$ depends on N, K, S, and θ_0. Fortunately, the effect of each parameter is nearly independent of the others. Figure 13.6 illustrates the relationship between S and K for $\theta_0 = 0°$, where $N = \lceil 20\lambda_c/S\rceil$ so that the averages are over $20\lambda_c$ (and $\lceil x\rceil$ denotes the smallest integer greater than or equal to x). Increasing N for a fixed S will increase the spatial averaging distance, thereby lowering the 1 σ spread in a manner similar to analog averaging in Fig. 13.4. The discontinuities in Fig. 13.6 are due to the $\lceil x\rceil$ function. Observe that if $S < 0.5\lambda_c$, then the discrete local mean estimate is approximately equivalent to the estimate from analog averaging ($\theta_0 = 0°$ in Fig. 13.5) over the same spatial distance. Similar to Fig. 13.5, it is also observe that small Rice factors, e.g., $K = 0.1$ and $K = 1$, at $\theta_0 = 0°$ increase the 1 σ spread. The spikes at $0.5\lambda_c$ and $1\lambda_c$ correspond to the location of the first lobe of the autocovariance function given by (2.94) and plotted in Fig. 2.16.

Although it is often assumed that $\theta_0 = 0°$ in our treatment, Fig. 13.7 shows the relationship between the 1 σ spread and S, for $K = 1$, $N = \lceil 20\lambda_c/S\rceil$, and several values of θ_0. Increasing θ_0 generally lowers the 1 σ spread except for some small angles as shown in Fig. 13.5; it also shifts the spike at $0.5\lambda_c$ to the right, because the first side lobe of (2.94) shifts as θ_0 increases.

To summarize, the spatial averaging distance that is needed to obtain the local mean depends on K and θ_0. If sample averaging is used, then the sample spacing should be less than $0.5\lambda_c$. As a rule of thumb, a spatial averaging distance of $20\lambda_c$ should be sufficient for most applications.

13.4 Velocity Estimation

Temporal based hard handoff algorithms can yield poor handoff performance in microcells due to the diverse propagation environment and the wide range of MS velocities. Consider the NLoS handoff scenario shown in Fig. 13.1, where a MS traveling from BS_0 has a log-normal shadowed Ricean faded LoS signal from BS_0 and a log-normal shadowed Rayleigh faded NLoS signal from BS_1, until it rounds the corner where the situation is suddenly reversed. The loss (gain) of the LoS component causes a rapid decrease (increase) in the signal strength. Effective hard handoff algorithms for this scenario should use short temporal averaging window and a large hysteresis, so that rapid changes in the mean signal strength are detected and unnecessary handoffs are prevented [233]. Unfortunately, temporal averaging with a short fixed window length gives optimal handoff performance for only a single velocity. For example, consider again the handoff scenario in Fig. 13.1

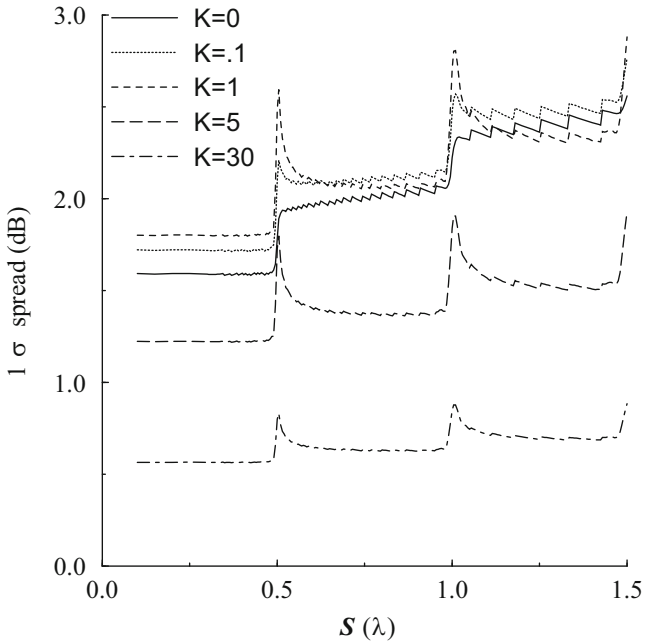

Fig. 13.6 1 σ spread versus S for various K, with $\theta_0 = 0°$, distance averaged = $20\lambda_c$, from [28]

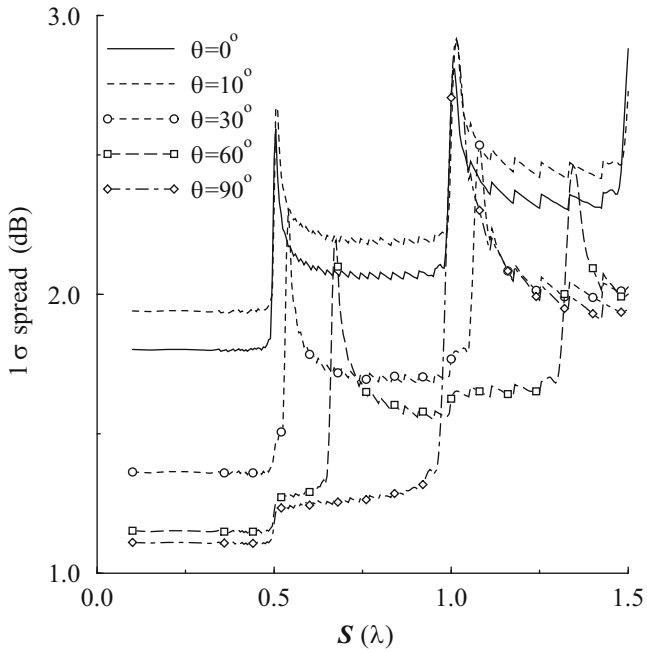

Fig. 13.7 1 σ spread versus S (in wavelengths) for various θ_0, $K = 1$, distance averaged = $20\lambda_c$, from [28]

along with the received signal strength profile in Fig. 2.67. Assume log-normal shadowing with $\sigma_\Omega = 6$ dB and choose D so that $\phi_{\Omega_{(\mathrm{dB})}\Omega_{(\mathrm{dB})}}(d) = 0.1\sigma_\Omega^2$ at $d = 30$ m in (2.6.1). The simulation of a temporal power averaging hard handoff algorithm with a hysteresis $H = 8$ dB, averaging window duration of 2.27 s, and a window overlap of $2.27/2 = 1.135$ s gives the handoff performance shown by the lines in Fig. 13.13.[2] The hard handoff performance is evaluated by the mean number of

[2] A 2.27 s window corresponds to a $20\lambda_c$ spatial window at a velocity of 5 km/h, assuming a carrier frequency of 1.9 GHz. Section 13.5 further details the simulation.

handoffs, averaged over 1000 runs, versus the distance from BS_0 where 50% (and 90%) of the MSs have made a handoff to BS_1, i.e., $Pr(BS_1) = 0.5$ and $Pr(BS_1) = 0.9$ at the abscissa. This distance gives a measure of the handoff delay, assuming that handoffs will occur between BS_0 and BS_1 only.

Figure 13.13 only shows the handoff request delay, while in a real system the network delay should also be included. However, the performance of a velocity adaptive handoff algorithm can still be evaluated without knowledge of the network delay. For example, suppose that the receiver threshold is -90 dBm. Also, assume that a good hard handoff algorithm should have at least 90% of the MSs handed off before a distance d_{cutoff}, where d_{cutoff} is chosen as the distance where the mean signal strength is $2\sigma_\Omega$ above -90 dBm. If $\sigma_\Omega = 6$ dB and the data from Fig. 2.67 is used, then a signal strength of $-90 + 12 = -78$ dBm occurs at 283 m for BS_0. Hence, if the velocity adaptive hard handoff algorithm can adapt to the point at 5 km/h in Fig. 13.13, corresponding to handoff requests at a distance 262 m, and the maximum speed of a MS turning the corner is 40 km/h (40/3.6 m/s), then a maximum network delay of

$$\text{Max Network Delay} = \frac{3.6\text{ s}}{40\text{ m}}(283 - 262)\text{ m} = 1.89\text{ s}$$

can be tolerated. For macrocellular systems this network delay is acceptable, implying the usefulness of velocity adaptive hard handoff algorithms discussed here. In the above example the 5 km/h point on the curve in Fig. 13.13 was chosen as the desired operating point, because the best hard handoff performance occurs near the knee of the curve where the mean number of handoffs and handoff delay are jointly minimized. Other hysteresis and window lengths could possibly result in better performance. However, the settings used here ($H = 8$ dB and a $20\lambda_c$ spatial window) are adequate to illustrate the usefulness of velocity adaptive hard handoff algorithms.

Hierarchical cellular architectures use microcells to serve high density low mobility MSs and macrocells to serve low density high mobility MSs. Velocity estimation is necessary so that MSs can be assigned to the proper hierarchical layer depending on their mobility. If high mobility MSs are connected to microcells, then excessive handoffs may occur. On the other hand, if low mobility MSs are connected to macrocells, then the overall system capacity will suffer. Finally, for hierarchical TDMA cellular architectures the micro-to-macrocell and micro-to-microcell handoffs must be performed quickly to prevent dropped calls, especially for MSs that are connected to microcells and subsequently transition from low to high mobility. For these cases, velocity adaptive handoff algorithms are necessary to achieve the required low network handoff delay.

13.4.1 Level Crossing Rate Estimators

It is well known that the zero crossing rates of the quadrature components $g_I(t)$ and $g_Q(t)$ and the level crossing of the envelope $\alpha(t) = |g(t)| = |g_I(t) + jg_Q(t)|$ are functions of the MS velocity as discussed in Sect. 2.1.5. The envelope level crossing rate (LCR) is defined as the average number of positive going crossings per second, that the fading envelope $\alpha(t)$ makes at a predetermined envelope level R. Likewise, the zero crossing rate (ZCR) is defined as the average number of positive going zero crossings of the quadrature components $\hat{g}_I(t) = g_I(t) - m_I(t)$ and $\hat{g}_Q(t) = g_Q(t) - m_Q(t)$. Rice has derived the ZCR of $\hat{g}_I(t)$ or $\hat{g}_Q(t)$ as (2.112)

$$L_{\text{ZCR}_1} = \frac{1}{\pi}\sqrt{\frac{b_2}{b_0}} \tag{13.20}$$

and the envelope LCR with respect to the level R as, (2.100) and (2.101),

$$L_R = \int_0^\infty \dot{\alpha} p(R, \dot{\alpha})\mathrm{d}\dot{\alpha} = \frac{R(2\pi)^{-3/2}}{\sqrt{Bb_0}} \int_0^\infty \int_{-\pi}^{\pi} \dot{\alpha} \tag{13.21}$$
$$\times \exp\left\{-\frac{1}{2Bb_0}\left(B\left(R^2 - 2Rs\cos(\theta) + s^2\right) + \left(b_0\dot{\alpha} + b_1 s\sin(\theta)\right)^2\right)\right\} \mathrm{d}\theta\mathrm{d}\dot{\alpha},$$

where $B = b_0 b_2 - b_1^2$. The b_n can be obtained from (2.103) with appropriate modification to account for the presence of additive white Gaussian noise in the received complex envelope. That is, the LCR is computed from the quadrature components of the received complex envelope $\tilde{r}_I(t) = g_I(t) + \tilde{n}_I(t)$ and $\tilde{r}_Q(t) = g_Q(t) + \tilde{n}_Q(t)$ instead of the quadrature components of the received fading envelope $g_I(t)$ and $g_Q(t)$. If an isotropic antenna is assumed such that $G(\theta) = 1$, then

$$b_n = (2\pi)^n b_0 \int_0^{2\pi} \hat{p}(\theta)(f_m \cos(\alpha) - f_q)^n \mathrm{d}\theta + (2\pi)^n \int_{-B_w/2}^{B_w/2} \frac{N_o}{2} f^n \mathrm{d}f, \tag{13.22}$$

where $2b_0$ is the scatter power, v is the velocity, λ_c is the carrier wavelength, $f_m = v/\lambda_c$ is the maximum Doppler frequency, $f_s = f_c + f_q$ is the frequency of the specular or LoS component, and $\hat{p}(\theta)$ is the continuous AoA distribution of the *scatter* component of the arriving plane waves [171]. The second term in (13.22) is due to additive white Gaussian noise (AWGN), centered at f_c, with a two-sided power spectral density of $N_o/2$ watts/Hz and a noise bandwidth of B_w Hz, resulting in a total power of $N_o B_w$ watts. Note that B_w is determined by the receiver bandwidth and must be at least equal to the maximum Doppler frequency f_m in order to accurately estimate the LCR. However, if B_w is larger than f_m, then the LCR estimates will be corrupted by unnecessary noise. For the special case when $\theta_0 = 0°$ and there is 2-D isotropic scattering, then $\hat{p}(\theta) = 1/(2\pi)$, $-\pi \le \theta \le \pi$ and (13.22) can be written as

$$b_n = (2\pi)^n \frac{b_0}{\pi} \int_{-f_m}^{f_m} \frac{f^n}{\sqrt{f_m^2 - f^2}} \mathrm{d}f + (2\pi)^n \int_{-B_w/2}^{B_w/2} \frac{N_0}{2} f^n \mathrm{d}f. \tag{13.23}$$

With Aulin's Ricean fading model with the means of $g_I(t)$ and $g_Q(t)$ defined in (2.59) and (2.60), respectively, the ZCR of $g_I(t)$ or $g_Q(t)$ is [283]

$$L_{\mathrm{ZCR}_2} = L_{\mathrm{ZCR}_1} \left(\mathrm{e}^{-\gamma} I_0(\beta) + \frac{b^2}{2\gamma} I_e\left(\frac{\beta}{\gamma}, \gamma\right) \right), \tag{13.24}$$

where $I_0(x)$ is the zero-order modified Bessel function of the first kind, and

$$\gamma = \frac{a^2 + b^2}{4}, \quad \beta = \frac{a^2 - b^2}{4}, \quad a = \sqrt{2K}$$
$$I_e(k, x) = \int_0^x \mathrm{e}^{-u} I_0(ku) \mathrm{d}u, \quad b = 2\pi f_m \cos(\theta_0) \sqrt{\frac{2Kb_0}{b_2}}, \tag{13.25}$$

and L_{ZCR_1} was defined in (13.20).

For macrocells, 2-D isotropic scattering is a reasonable assumption. However, for microcells the scattering is often non-isotropic. Nevertheless, one approach is to derive velocity estimators under the assumption of 2-D isotropic scattering with no AWGN, and afterwards study the effects of the mismatch caused by non-isotropic scattering and noise. Using (13.20) along with the definition for the b_n in (13.23) and $N_o = 0$ gives

$$L_{\mathrm{ZCR}_1} = \sqrt{2} v/\lambda_c \tag{13.26}$$

and (2.109)

$$L_R = (v/\lambda_c)\sqrt{2\pi(K+1)}\rho \mathrm{e}^{-K-(K+1)\rho^2} I_0\left(2\rho\sqrt{K(K+1)}\right), \tag{13.27}$$

where $\rho = R/R_{\mathrm{rms}}$, where $R_{\mathrm{rms}} = \sqrt{\Omega_p}$ is the rms envelope level. Likewise, for Aulin's Ricean fading model with the means in (2.59) and (2.60), and $\theta_0 = 0°$,

$$\gamma = \frac{3K}{2}, \quad \beta = -\frac{K}{2}, \quad a = \sqrt{2K}, \quad b = 2\sqrt{K}, \tag{13.28}$$

and L_{ZCR_2} reduces to

$$L_{\mathrm{ZCR}_2} = (v/\lambda_c)\sqrt{2}\left(\mathrm{e}^{-3K/2} I_0\left(-\frac{K}{2}\right) + \frac{4}{3} I_e\left(-\frac{1}{3}, \frac{3K}{2}\right)\right). \tag{13.29}$$

Clearly, the LCR and ZCR are proportional to the velocity v and, hence, can be used to derive a velocity estimate. However, it remains to be seen if they are robust to the Rice factor K, non-isotropic scattering, additive noise, and other factors. The robustness with respect to K is first considered, and the other factors are treated afterwards.

L_{ZCR_1} is not affected by K. Figure 2.17 in Sect. 2.1.5 compared the level crossing rate L_R for different K with the conclusion that the LCR around $\rho = 0\,\mathrm{dB}$ is roughly independent of K. This attractive property suggests that the LCR can be used to provide a velocity estimate that is robust to K. Consequently, the steps for using the LCR (or ZCR) of $\alpha(t)$ (or $g_I(t)$ or $g_Q(t)$) for velocity estimation are; determine R_{rms} (or $m_I(t)$ or $m_Q(t)$), estimate the number of crossings per second $\hat{L}_{R_{\mathrm{rms}}}$ (or $\hat{L}_{\mathrm{ZCR}_1}$), and use (13.27) to solve for v, with $\rho = 1$ and $K = 0$ (or (13.26) for ZCR_1). Thus, the following velocity estimators are robust with respect to Rice factor K:

$$\hat{v}_{\mathrm{ZCR}_1} \approx \frac{\lambda_c \hat{L}_{\mathrm{ZCR}}}{\sqrt{2}}, \quad \hat{v}_{\mathrm{LCR}} \approx \frac{\lambda_c \hat{L}_{\mathrm{R_{rms}}}}{\sqrt{2\pi}\,\mathrm{e}^{-1}}. \tag{13.30}$$

Figure 13.8 shows the effect of K and θ_0 on L_{ZCR_2}. Notice that if the angle of the specular component is $\theta_0 = 0°$ or 180°, then L_{ZCR_2} can have up to 40% relative error. Consequently, a non-zero value of K should be chosen as a default value to minimize the effect of K. Choosing $K \approx 0.61$ yields a maximum error of at most 20%. In this case, the velocity estimate from (13.29) becomes

$$\hat{v}_{\mathrm{ZCR}_2} \approx \frac{\lambda_c \hat{L}_{\mathrm{ZCR}_2}}{1.2\sqrt{2}}. \tag{13.31}$$

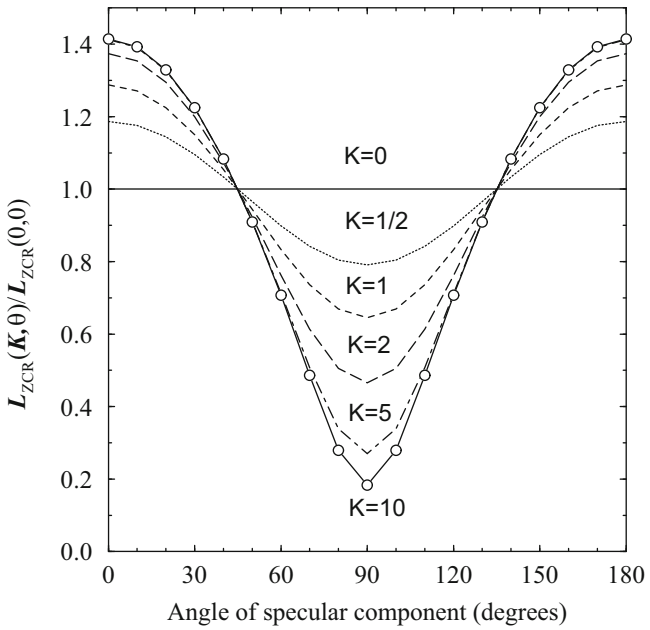

Fig. 13.8 Normalized zero crossing rate versus K and θ_0, from [28]

13.4.2 Covariance Approximation Methods

A velocity estimator has been proposed by Holtzman and Sampath [167, 288] that relies upon an estimate of the autocovariance between faded samples $r[i]$, where the $r[i]$ can be samples of the envelope, squared-envelope, or log-envelope. With this method, referred to here as the covariance (COV) method, the statistic

$$V = \frac{1}{N}\sum_{k=1}^{N}(r[k+\tau] - r[k])^2 \tag{13.32}$$

is calculated. If N is large and ergodicity applies, then V can be replaced by the ensemble average

$$\mathrm{E}[V] = 2\lambda_{rr}(0) - 2\lambda_{rr}(\tau), \tag{13.33}$$

where $\lambda_{rr}(\tau)$ denotes the autocovariance of $r[k]$. The general form for $\lambda_{rr}(\tau)$, assuming squared-envelope samples, can be derived from [22] and [288] as

$$\begin{aligned}\lambda_{rr}(\tau) = {} & 4a(\tau)\Big(a(\tau) + s^2 \cdot \cos(2\pi f_m \tau \cos(\theta_0))\Big) + 4c^2(\tau) + \frac{2N_o a(\tau)\sin(B_w \pi \tau)}{\pi\tau} \\ & + \frac{4KN_o b_0 \cos(2\pi f_m \tau \cos(\theta_0))\sin(B_w\pi\tau)}{\pi\tau} + \frac{{N_o}^2 \sin(B_w\pi\tau)^2}{\pi^2\tau^2},\end{aligned} \tag{13.34}$$

where [22]

$$a(\tau) = b_0 \int_0^{2\pi} \hat{p}(\theta)\cos\left(2\pi f_m \tau\cos(\theta)\right)\mathrm{d}\theta \tag{13.35}$$

$$c(\tau) = b_0 \int_0^{2\pi} \hat{p}(\theta)\sin\left(2\pi f_m \tau\cos(\theta)\right)\mathrm{d}\theta. \tag{13.36}$$

This estimator depends on $\hat{p}(\theta)$ and, hence, is also a function of the scattering environment. Like the LCR estimator, isotropic scattering is first assumed without additive noise to derive a velocity estimator and afterwards the effect of non-isotropic scattering and noise is considered.[3] Consider the scattering environment shown in Fig. 2.7, characterized by 2-D isotropic scattering plus a LoS or specular component arriving at angle $\theta_0 = \pi/2$. If squared-envelope samples are used, then using (2.94) gives

$$\overline{V} = \mathrm{E}[V] = 2\left(\frac{\Omega_p}{K+1}\right)^2\Big((1+2K) - J_0(2\pi f_m\tau)\Big(J_0(2\pi f_m\tau) + 2K\cos(2\pi f_m\tau\cos(\theta_0))\Big)\Big), \tag{13.37}$$

which is dependent on K and θ_0. If $\lambda_{rr}(0)$ is known exactly, then the bias with respect to K can be eliminated for small τ by the normalization [288]

$$\frac{\overline{V}}{\lambda_{rr}(0)} \approx (2\pi v\tau_t/\lambda_c)^2\frac{1+2K+K\cos(2\theta_0)}{(1+2K)} \tag{13.38}$$

so that [288]

$$\hat{v}_{\mathrm{COV}} \approx \frac{\lambda_c}{2\pi\tau_t}\sqrt{\frac{\overline{V}}{\lambda_{rr}(0)}}, \tag{13.39}$$

where τ_t is the sample spacing in seconds/sample.

[3] Only isotropic scattering was considered in [167, 288].

In large co-channel interference situations it may be preferable to modify the above scheme since the empirical average in (13.32), and in particular $\lambda_{rr}(0)$, is sensitive to co-channel interference as shown in [183]. Consequently, defining

$$U(\tau) = \frac{1}{N}\sum_{k=1}^{N} r[k+\tau]r[k] - \left(\frac{1}{N}\sum_{k=1}^{N} r[k]\right)^2 \tag{13.40}$$

and $V_2 = 2U(\tau_1) - 2U(\tau_2)$, yields

$$\mathrm{E}[V_2] = 2\lambda_{rr}(\tau_1) - 2\lambda_{rr}(\tau_2) \tag{13.41}$$

so that $\mathrm{E}[V_2]/\lambda_{rr}(0)$ is equal to (13.38) with $\tau_t = \tau_2^2 - \tau_1^2$, and a result similar to (13.39) follows.

Whether V or V_2 is used, $\lambda_{rr}(0)$ is never known exactly and must be estimated by the MS in the same way that $m_I(t)$, $m_Q(t)$, and R_{rms} must be estimated in the ZCR and LCR methods, respectively. Consequently, to actually use (13.39) it must be shown or verified that

$$v \propto \mathrm{E}\left[\sqrt{\frac{\overline{V}}{\lambda_{rr}(0)}}\right]. \tag{13.42}$$

This is analytically difficult, but simulation results in Sect. 13.5 suggest that (13.39) is a useful approximation to (13.42).

It is also shown in Appendix 13A that

$$\lim_{\tau\to 0}\hat{v}_{\mathrm{COV}} = \lim_{\tau\to 0}\frac{\lambda_c}{2\pi\tau}\sqrt{\frac{\overline{V}}{\lambda_{rr}(0)}} = v\sqrt{\frac{1+2K+K\cos(2\theta_0)}{1+2K}}. \tag{13.43}$$

It follows from (13.39) and (13.43) that K and θ_0 cause at most 20% error in v [288], thus providing a velocity estimator that is reasonably robust with respect to K.

13.4.3 Velocity Estimator Sensitivity

To illustrate the sensitivity of the velocity estimators, the ratio of the corrupted velocity estimate to the ideal velocity estimate is used. For the LCR and ZCR velocity estimators,

$$\frac{\tilde{v}}{v} = \frac{\tilde{L}_{R_{\mathrm{rms}}}(\tilde{b}_0, \tilde{b}_1, \tilde{b}_2)}{L_{R_{\mathrm{rms}}}(b_0, b_1, b_2)} \tag{13.44}$$

and

$$\frac{\tilde{v}}{v} = \frac{\tilde{L}_{\mathrm{ZCR}_1}}{L_{\mathrm{ZCR}_1}} = \sqrt{\frac{\tilde{b}_2}{\tilde{b}_0}\cdot\frac{b_0}{b_2}}, \tag{13.45}$$

respectively, where $\tilde{v}$ denotes the corrupted velocity estimate, and the level crossing rates $\tilde{L}_{R_{\mathrm{rms}}}(\tilde{b}_0, \tilde{b}_1, \tilde{b}_2)$ and $L_{R_{\mathrm{rms}}}(b_0, b_1, b_2)$ are given by (13.21) with the appropriate values of $\tilde{b}_n$ and b_n, respectively. Little simplification results for the LCR method in general. However, when $K = 0$ (13.45) simplifies to [171]

$$\frac{\tilde{v}}{v} = \sqrt{\frac{\tilde{b}_2/\tilde{b}_0 - \tilde{b}_1^2/\tilde{b}_0^2}{b_2/b_0 - b_1^2/b_0^2}}. \tag{13.46}$$

For Aulin's fading model with the means in (2.59) and (2.60), the sensitivity of the ZCR is

$$\frac{\tilde{v}}{v} = \frac{\tilde{L}_{\mathrm{ZCR}_2}}{L_{\mathrm{ZCR}_2}} = \frac{\tilde{L}_{\mathrm{ZCR}_1}}{L_{\mathrm{ZCR}_1}}\cdot\frac{\mathrm{e}^{-\tilde{\gamma}}I_0(\tilde{\beta}) + \frac{\tilde{b}^2}{2\tilde{\gamma}}I_e\left(\frac{\tilde{\beta}}{\tilde{\gamma}}, \tilde{\gamma}\right)}{\mathrm{e}^{-\gamma}I_0(\beta) + \frac{b^2}{2\gamma}I_e\left(\frac{\beta}{\gamma}, \gamma\right)}, \tag{13.47}$$

where $\tilde{\beta}$, $\tilde{\gamma}$, and $\tilde{b}$ are given by (13.25) using (13.22) where appropriate. Likewise, for the covariance method using squared-envelope samples,

$$\frac{\tilde{v}}{v} = \frac{\sqrt{\frac{2\tilde{\lambda}_{rr}(0) - 2\tilde{\lambda}_{rr}(\tau)}{\tilde{\lambda}_{rr}(0)}}}{\sqrt{\frac{2\lambda_{rr}(0) - 2\lambda_{rr}(\tau)}{\lambda_{rr}(0)}}}. \tag{13.48}$$

13.4.3.1 Effect of the Scattering Distribution

Here the sensitivity of the velocity estimators to the scattering distribution is studied by using four different non-isotropic scattering models. With the first model S1, plane waves arrive from one direction only with a varying degree of directivity as might happen when signals are channelized along a city street. The probability density of the scatter component of the arriving plane waves as a function of angle of arrival has the form in (2.52), where the vehicle motion is in the direction of $\theta = 0°$, and θ_m determines the directivity of the incoming plane waves. Figure 2.9 shows a polar plot of $\hat{p}(\theta)$ for $\theta_m = 30°, 60°$, and $90°$. The second model S2 assumes that the plane waves can arrive from either the front ($\theta = 0°$) or back ($\theta = 180°$), which may be typical for city streets that dead end at another street. In this case $\hat{p}(\theta)/2$ and $\hat{p}(\theta - \pi)/2$ are combined to form the overall angle-of-arrival distribution. The resulting density is similar to Fig. 2.9 but with lobes extending in both the 0° and 180° directions. The third and fourth models S3 and S4, respectively, are similar to S1 and S2 except that the distributions are rotated by 90°, so that the plane waves tend to arrive perpendicular to the direction of travel. This may occur when a MS passes through a street intersection. The effect of the scattering distribution is determined for the cases when the velocity estimator has been designed for (1) isotropic scattering and, (2) scattering model S1 with $\theta_m = 90°$. The scattering model that the velocity estimator has been designed for will determine the values of b_0, b_1, and b_2 in the denominators of (13.44)–(13.47), while the values of $\tilde{b}_0$, $\tilde{b}_1$, and $\tilde{b}_2$ depend on the scattering environment that is actually present. The effect of non-isotropic scattering on the COV estimate (13.48) can be found from the results in Appendix 13A with $N_o = 0$, or by using small values of τ in (13.48). Here, the latter is chosen with $\tau = 1/50$.

Figure 13.9 shows the effect of the scattering distribution on each of the velocity estimators. Due to the very large number of possible scenarios, only the most significant results are plotted in Fig. 13.9 and curves similar (but not equal) to the plotted curves are simply asterisked in the accompanying table. Velocity estimators with the subscript "d" in Fig. 13.9 correspond to those that are designed for scattering model S1 with $\theta_m = 90°$. By using Fig. 13.9 the relative robustness of the various velocity estimators to the scattering distribution has been summarized by the ranking in Table 13.1.

For urban microcell deployments, robustness with respect to scattering models S1 and S2 is important. The LCR and COV methods are very sensitive to the directivity in scattering model S1 when $K = 0$ as shown by curve "h." This sensitivity can be partially mitigated by using the velocity estimators LCR_d and COV_d that have been designed for scattering model S1 with $\theta_m = 90°$ as shown by curve "g." However, the price for increased robustness to scattering model S1 is the increased sensitivity of LCR_d to scattering models S2, S3, and S4 when $K = 0$. Fortunately, the presence of even a small specular component ($K = 1$) reduces the sensitivity as seen in COV ($K = 1$) and LCR_d. In contrast a specular component does not reduce the sensitivity of the LCR estimator in scattering models S2, S3, and S4, because $b_1 = 0$, and therefore the ratio of the crossing rates in (13.46) depends on $\tilde{b}_2$ and b_2 and is independent of K. Results are not shown for LCR or LCR_d with $K = 1$ scattering model S1, due to numerical difficulties in calculating (13.21) for small θ_m. For large $\theta_m > 80°$ the results obtained were very close to curve "d."

The ZCR velocity estimator is generally more robust than the LCR and COV methods. The presence of a small specular component improves robustness to the scattering distribution as seen in ZCR_2, $\text{ZCR}_{2,d}$ (ZCR_1 and ZCR_{1_d} are independent of K). Also, velocity estimators that have been designed for scattering model S1 with $\theta_m = 90°$ perform slightly better than those designed for isotropic scattering. However, the improvement obtained by using these velocity estimators must be weighed against the relative error that will be introduced if the scattering is actually isotropic. For LCR_d and COV_d, $\tilde{v}/v = 0.316$ and for ZCR_d $\tilde{v}/v = 1.15$. Since all the velocity estimators seem to have some sensitivity to the scattering distribution, and sensitivity is greatly reduced when $K > 0$, we conclude that those designed for isotropic scattering should be adequate.

In summary, for very directive situations where the plane waves arrive from either the front or back but not both, the ZCR, COV_d, or LCR_d methods are the most robust. If the plane waves arrive from both the front and back, then all the velocity estimators with the exception of LCR_d are reasonably robust. The sensitivity to directivity is reduced when a specular component is present. In the unlikely event that $K = 0$ and plane waves arrive from the perpendicular direction with high directivity, all methods will have a significant bias. Finally, another method for overcoming the sensitivity to the scattering distribution is to obtain velocity estimates from the signals that arrive at a MS from a distant cell or an umbrella cell, since they will tend to experience 2-D isotropic scattering.

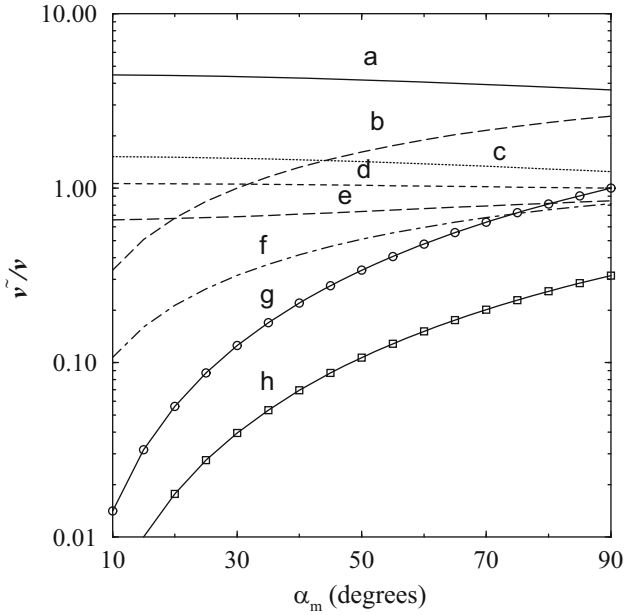

	Scattering model							
	1		2		3		4	
Method	$K=0$	$K=1$	$K=0$	$K=1$	$K=0$	$K=1$	$K=0$	$K=1$
LCR	h	—	c*	c*	f	f	f	f
LCR_d	g	—	a	c	b	f*	b	f*
ZCR_1	c*	c*	c*	c*	f	f	f	f
ZCR_{1d}	d*	d*	d*	d*	f*	f*	f*	f*
ZCR_2	c*	d*	c*	d*	f	d*	f	d*
ZCR_{2d}	d*	d	d*	d	f*	d*	f*	d*
COV	h	d*	c*	d*	f	e*	f	e*
COV_d	g	d*	a	d*	b	e	b	e

Fig. 13.9 Non-isotropic scattering effects.—corresponds to a curve that had insufficient precision to be reported. Superscript x^* denotes that the curve is approximately equal the curve labeled x, from [28]

Table 13.1 Robustness to the scattering distribution

Curve	Rank	$\tilde{v}/v$ at $\theta_m = 10°$	$\tilde{v}/v$ at $\theta_m = 90°$
d	Excellent	1.06	1.0
e, c	Very good	0.66, 1.52	0.85, 1.24
b, f	Good	0.34, 0.107	2.6, 0.82
a, g, h	Poor	4.5, 0.014, 0.004	3.6, 1.0, 0.32

13.4.3.2 Effects of Additive Gaussian Noise

Since the effect of the scattering distribution has already been established, the sensitivity to additive white Gaussian noise (AWGN) is determined by using Eqs. (13.44) to (13.48) under the assumption of 2-D isotropic scattering. With AWGN the rms value of the received complex envelope is $\tilde{R} = \sqrt{s^2 + 2b_0 + N_o B_w}$, and the values of $\tilde{b}_n$ and b_n in (13.44) are

$$\tilde{b}_0 = b_0 + \frac{N_o B_w}{2} \tag{13.49}$$

$$\tilde{b}_2 = 2b_0 (\pi f_m)^2 + \frac{N_o B_w^3 \pi^2}{6} \tag{13.50}$$

$$b_2 = 2b_0 (\pi f_m)^2 . \tag{13.51}$$

For the LCR velocity estimator, (13.44) and (13.21) yield, after considerable algebra,

$$\frac{\tilde{v}}{v} = \left(1 + \frac{K+1}{6\gamma_S}\left(\frac{B_w}{f_m}\right)^2\right)^{\frac{1}{2}} \frac{\sqrt{\gamma_S(\gamma_S+1)}}{\gamma_S+K+1} \frac{I_0\left(\frac{2\sqrt{\gamma_S(\gamma_S+1)K(K+1)}}{\gamma_S+K+1}\right)}{I_0\left(2\sqrt{K(K+1)}\right)} \exp\left\{2K+1-\frac{\gamma_S(2K+1)+K+1}{\gamma_S+K+1}\right\}, \quad (13.52)$$

where

$$\gamma_S \triangleq \frac{s^2+2b_0}{N_o B_w} = \frac{\Omega_p}{N_o B_w} \quad (13.53)$$

is defined as the signal-to-noise ratio. Likewise, for the ZCR velocity estimator ZCR_1, (13.45) becomes

$$\frac{\tilde{v}}{v} = \sqrt{\frac{\gamma_S + \left(\frac{B_w}{f_m}\right)^2 \frac{K+1}{6}}{\gamma_S+K+1}}. \quad (13.54)$$

For Aulin's fading model with the means in (2.59) and (2.60), the effect of AWGN on ZCR_2 can be obtained from (13.47) with $\tilde{L}_{\mathrm{ZCR}_1}/L_{\mathrm{ZCR}_1}$ in (13.54),

$$\tilde{\beta} = \frac{K}{2}\left(1 - 2\cos^2(\theta_0)\left(\frac{\gamma_S+K+1}{\gamma_S + \frac{K+1}{6}\left(\frac{B_w}{f_m}\right)^2}\right)\right) \quad (13.55)$$

$$\tilde{\gamma} = \frac{K}{2}\left(1 + 2\cos^2(\theta_0)\left(\frac{\gamma_S+K+1}{\gamma_S + \frac{K+1}{6}\left(\frac{B_w}{f_m}\right)^2}\right)\right) \quad (13.56)$$

$$\tilde{b} = 2\sqrt{K}\cos(\theta)\sqrt{\frac{\gamma_S+K+1}{\gamma_S + \frac{K+1}{6}\left(\frac{B_w}{f_m}\right)^2}} \quad (13.57)$$

and a, b, γ, and β given by (13.28).

In [288], the effect of AWGN on the COV velocity estimator has been derived as a function of $\tau > 0$. Here a closed form analytic result is provided for the effect of AWGN on the COV velocity estimate for the limiting case when $\tau \to 0$. The limiting case is important when analyzing the effects of AWGN, since (13.38) is only valid for small τ. Consequently, the $\lim_{\tau\to 0} \tilde{v}/v$ in (13.48) is found, and afterwards, the effect of $\tau > 0$ in (13.48) is compared. It is shown in Appendix 13A that

$$\lim_{\tau\to 0} \tilde{v}/v = \frac{\sqrt{\zeta}}{\sqrt{\frac{(1+2K+K\cos(2\theta_0))}{(1+2K)}}}, \quad (13.58)$$

where ζ is given by (13A.4), with $a(0) = b_0, a'(0) = c(0) = c'(0) = c''(0) = 0$ and $a''(0) = 2b_0(\pi f_m)^2$ for 2-D isotropic scattering.

It is apparent from (13.52), and (13.54)–(13.58) that the effect of AWGN depends on K, B_w, γ_S, v, and θ_0. For a practical system, the bandwidth B_w can be chosen as the maximum expected Doppler frequency over the range of velocities. However, a smaller B_w in reference to the actual maximum Doppler frequency f_m will result in velocity estimates that are less sensitive to noise. Therefore, a better approach is to use the velocity estimate $\hat{v}$ to continuously adjust B_w to be just greater than the current maximum Doppler frequency, i.e., $B_w \gtrsim \hat{v}/\lambda_c$. Figure 13.10 shows the effect of AWGN on each of the velocity estimators with respect to K, γ_S, and v, assuming $\theta_0 = 0°$ (head-on LoS specular component). A value of $B_w = 357$ Hz is chosen which allows speeds up to 100 km/h at $f_c = 1.9$ GHz. For $K = 0$, AWGN has the same effect on all the velocity estimators. For larger velocities, e.g., 20 km/h, the bias becomes insignificant because B_w/f_m is small. However, for small velocities, e.g., 1 km/h, a very large B_w/f_m results in a significant bias. As mentioned above, this slow speed bias can be reduced by adapting the filter bandwidth B_w. It must also be remembered that Fig. 13.10 shows the worst case performance of the COV method as $\tau \to 0$. Any $\tau > 0$ will reduce the bias of the COV method due to AWGN. For example, if $2\pi v\tau/\lambda_c = 0.5$ in (13.48), then

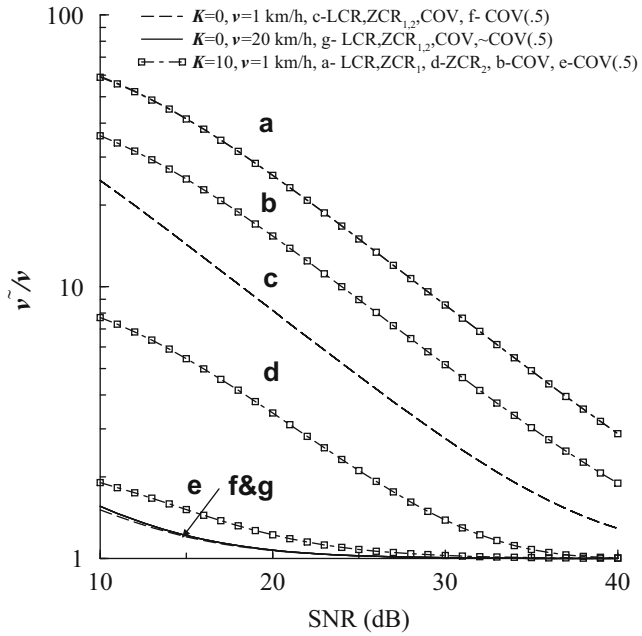

Fig. 13.10 The effect of AWGN on the velocity estimates. COV(0.5)$\Rightarrow 2\pi v\tau/\lambda_c = 0.5$, from [28]

a large reduction in the effect of AWGN is realized, as shown by the curves labeled COV(0.5) in Fig. 13.10. However, the accuracy of the COV velocity estimate itself improves with smaller τ, so that increasing τ for reduced noise sensitivity must be weighed against the reduced accuracy of the velocity estimate itself. This will be discussed further in the next section.

13.5 Velocity Adaptive Hard Handoff Algorithms

To study velocity adaptive handoff algorithms Rayleigh fading ($K = 0$) is assumed, 2-D isotropic scattering, and no AWGN. A velocity adaptive handoff algorithm must adapt the temporal window over which the mean signal strength estimates are taken by either keeping the sampling period constant and adjusting the number of samples per window, or vice versa. Here, the latter is assumed. To reduce the variance in the velocity estimate, a sum of weighted past velocity estimates is performed using an exponential window average of past estimates, i.e.,

$$\check{v}(n) = a\check{v}(n-1) + (1-a)\hat{v}(n), \tag{13.59}$$

where a controls the weighting of past estimates used in the average, and $\hat{v}(n)$ is the current velocity estimate. The accuracy of the velocity estimates will be affected by the window length W_l used to obtain the velocity estimates (not to be confused with the window length over which the signal strengths are averaged), and the number of samples per wavelength N_λ.

To show the effect of parameters a, N_λ, and W_l, simulation of the NLoS handoff scenario shown in Fig. 13.1 along with the corresponding signal strength profile in Fig. 2.67 was performed. The path loss was assumed to follow the model in (2.412) with $a = 2$, $b = 2$, $g = 150$ m, and $d_c = 255$ m. Spatially correlated log-normal shadows were simulated having a standard deviation of $\sigma_\Omega = 6$ dB and $\zeta_{30} = 0.1$ using the approach in Sect. 2.6.1. Envelope fading was simulated using Jakes' method in Sect. 2.5.2.2. Two-branch receiver antenna diversity was assumed, so that the $\hat{v}(n)$ in (13.59) represent the average estimate out of the diversity branches at position n, and $a = 0.1$ in (13.59) unless otherwise specified.

As mentioned previously, Fig. 13.13 shows the performance of a temporal handoff algorithm with $H = 8$ dB, signal strength averaging over 2.27 s, and overlapping windows by $2.27/2 = 1.135$ s. Slightly better temporal handoff performance can probably be obtained by fine tuning these values. However, for purposes of studying the velocity adaptive algorithms it is sufficient to maintain $H = 8$ dB and adapt to some point near the knee of the performance curve. Consequently, the velocity estimators were designed to adapt to the 5 km/h operating point which corresponds to signal strength window averages over approximately $20\,\lambda_c$ with a window overlap of approximately $10\,\lambda_c$.

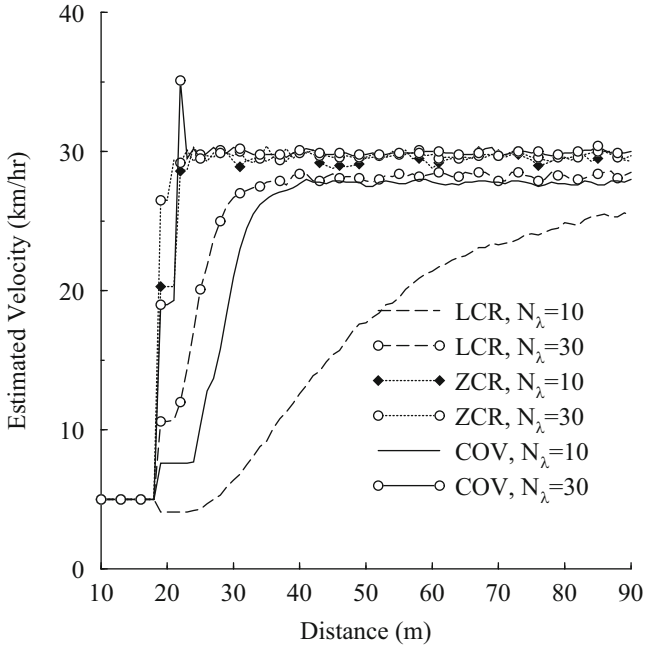

Fig. 13.11 The effect of N_λ on the mean response time to a change in velocity. $a = 0.1$, $W_l = 10\,\lambda_c$, from [28]

A total of 1000 runs were made from BS_0 to BS_1, and the 95% confidence intervals were calculated for (1) the velocity at 100 m, (2) the corner at 255 m, and (3) the probability of being assigned to BS_0 at 255 m. This resulted in a 95% confidence interval spread of $\hat{v} \pm 0.5$ km/h and $\Pr(BS_0)$ ± 0.025. Likewise, the mean number of handoff values had a 95% confidence interval spread of approximately 0.05 (mean number of handoffs ± 0.025).

13.5.1 Effect of N_λ

To examine the effect of N_λ, assume that $a = 0.1$ and $W_l = 10\,\lambda_c$ for the LCR, ZCR, and COV velocity estimators, and assume that the MS traverses the NLoS handoff route in Fig. 13.1 at 30 km/h. Furthermore, assume that the velocity estimators are initialized to 5 km/h, and that the MS is measuring signals from BS_0 and BS_1 only. Figure 13.11 shows the effect of N_λ on the velocity estimate, in the first 90 m of the trajectory as the MS moves from BS_0 to BS_1, in terms of the response time and final velocity estimate. The LCR velocity estimator requires a higher sampling density than the COV or ZCR methods and its final velocity and response time to an incorrect startup value (5 km/h) improve dramatically when N_λ is increased from 10 to 30 samples/wavelength. For $N_\lambda = 30$ the COV method shows a slight overshoot in the initial convergence, a characteristic seen with all the velocity estimators as the sampling density is increased. It is interesting to note that for $N_\lambda = 10$ samples/wavelength $2\pi(v\tau)/\lambda_c = 2\pi 0.1\lambda_c/\lambda_c = .628$ and the final COV velocity estimate is close to the actual 30 km/h with a reasonable response time. This fact, along with the results of Sect. 13.4.3.2 where $2\pi v\tau/\lambda_c = 0.5$ confirm that the effects of AWGN can be mitigated by using a larger sample spacing without drastically affecting the velocity estimate. The simulations used an estimate of the rms value R_{rms} in the LCR method and an estimate of the variance $\lambda_{rr}(0)$ in the COV method. Thus, the practicality of the velocity estimators that have been derived assuming perfect knowledge of these values is confirmed. Although not shown here, the Rice factor K has little effect, confirming the claimed robustness of the estimators. Over the 1000 runs, the ZCR had the smallest velocity estimate error variance followed by the COV and LCR methods, respectively.

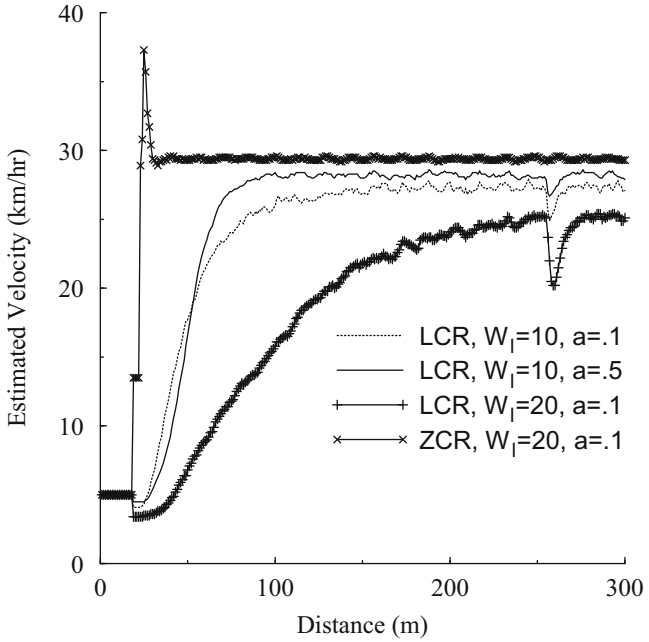

Fig. 13.12 The effect of a and W_l on the mean response and corner effects, from [28]

13.5.2 Corner Effects and Sensitivity to a and W_l

The sharp downward spike at the corner (255 m) for the LCR velocity estimate in Fig. 13.12 is typical of the corner effects on the velocity estimators. The effect is caused by a sudden change in path loss which lowers the local mean estimate in the LCR method thus yielding fewer level crossings per second. This corner effect is apparent, although less acute in the ZCR and COV methods due to their quick adaptability. The LCR and ZCR methods may exhibit a drop in estimated velocity when the average signal strength changes abruptly. Although not shown here, the COV method has an upward bias with an abrupt increase in the average signal strength, and a downward bias when the opposite occurs. These corner effect properties could possibly be exploited to provide a combined corner detecting velocity adaptive handoff algorithm [24].

Larger values of a reduce the variance of the velocity estimate while sacrificing response time. Smaller values of a provide faster startup convergence and more sensitivity to corner effects.

Although a velocity window length W_l less than $20\,\lambda_c$ will increase the variance of the velocity estimates, it is beneficial for reducing the corner effect on the velocity estimator, as shown for the LCR method. Although not shown, the same is true for the ZCR and COV methods. The ZCR curve with $W_l = 20\,\lambda_c$ and $a = 0.5$ shows an overshoot in the initial convergence. This arises because the $W_l = 20\,\lambda_c$ windows that are used to obtain the velocity estimates overlap by $10\,\lambda_c$. Hence, part of the velocity estimate is derived from the previous window which may have a different sampling period due to adaptation. Note that overlapped windows are used because they result in less handoff delay. Thus, it is probably better for initial startup to derive velocity estimates from the non-overlapped portions of the signal strength windows.

13.5.3 Velocity Adaptive Handoff Performance

Now that the effect of each parameter has been determined, the performance of the velocity adapted handoff algorithm is shown by the various symbols in Fig. 13.13 for a MS traveling at 30 km/h. The estimators were selected to adapt to the 5 km/h operating point, the algorithm parameters were chosen as $a = 0.1$, $W_l = 10\,\lambda_c$ with an initial startup velocity of 5 km/h. The mean number of handoffs was found to have a 95% confidence interval with a span of about 0.05 (mean number of handoffs ± 0.025) about the mean that is plotted. The velocity adaptive handoff algorithm performs very well by maintaining the desired operating point near the 5 km/h point.

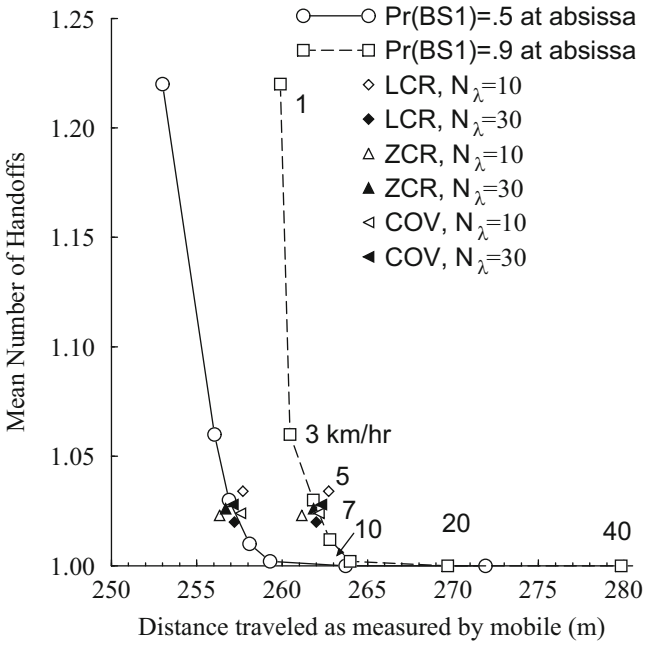

Fig. 13.13 Handoff performance of a 2.27 s averaging handoff algorithm in comparison with a velocity adaptive handoff algorithm using the LCR, ZCR, or covariance method for velocity control. $H = 8$ dB, $\sigma_\Omega = 6$ dB, from [28]

13.6 Hard Handoff Analysis

The classical signal strength based hard handoff algorithm compares signal strength averages measured over a time interval T (seconds), and executes a handoff if the average signal strength of the target BS is at least H dB larger than that of the serving BS [28, 150, 332, 333]. The analytical computation of the handoff characteristics for this classical signal strength based handoff algorithm is generally intractable. However, for the case when the average signal strength decays smoothly along a handoff route and the handoff hysteresis H is not too small compared to the shadow standard deviation, Vijayan and Holtzman [332, 333] have developed an analytical method to characterize the performance of the classical signal strength based handoff algorithm. They have also extended their results to include handoff algorithms that use absolute measurements [373], similar to the one in (13.4).

Consider the case of a MS moving at a constant velocity along a straight line between two BSs, BS_0 and BS_1, that are separated by a distance of D meters. Envelope fading is neglected under the assumption that the received signal strength estimates are averaged by using a window with an appropriate spatial length as explained in Sect. 13.3 and using velocity adaptive averaging as discussed in Sect. 13.5. In any case, however, the signal strength estimates will respond to path loss and shadowing variations. Considering the effects of path loss and shadowing, the signal levels $\Omega_{0\,(\mathrm{dB})}(d)$ and $\Omega_{1\,(\mathrm{dB})}(d)$ that are received from BS_0 and BS_1, respectively, are (1.4)

$$\Omega_{0\,(\mathrm{dB})}(d) = \Omega_{(\mathrm{dB})}(d_0) - 10\beta\log_{10}\{d/d_0\} + \epsilon_{0\,(\mathrm{dB})} \tag{13.60}$$

$$\Omega_{1\,(\mathrm{dB})}(d) = \Omega_{(\mathrm{dB})}(d_0) - 10\beta\log_{10}\{(D-d)/d_0\} + \epsilon_{1\,(\mathrm{dB})}, \tag{13.61}$$

where d is the distance between BS_0 and the MS. The parameters $\epsilon_{0\,(\mathrm{dB})}$ and $\epsilon_{1\,(\mathrm{dB})}$ are independent zero-mean Gaussian random processes with variance σ_Ω^2, reflecting a log-normal shadowing model. The signal strength measurements are assumed to be averaged by using an exponential averaging window with parameter d_{av} so that the averaged signal levels from the two BSs are, respectively,

$$\overline{\Omega}_{0\,(\mathrm{dB})}(d) = \frac{1}{d_{\mathrm{av}}}\int_0^d \Omega_{0\,(\mathrm{dB})}(d-x)\mathrm{e}^{-x/d_{\mathrm{av}}}\mathrm{d}x \tag{13.62}$$

$$\overline{\Omega}_{1\,(\mathrm{dB})}(d) = \frac{1}{d_{\mathrm{av}}}\int_0^d \Omega_{1\,(\mathrm{dB})}(d-x)\mathrm{e}^{-x/d_{\mathrm{av}}}\mathrm{d}x. \tag{13.63}$$

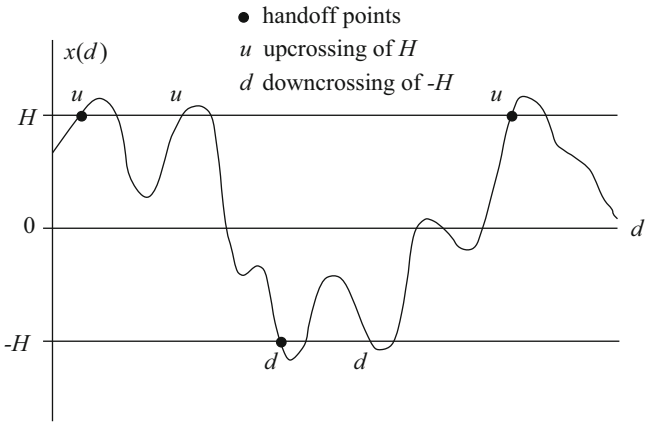

Fig. 13.14 Handoff initiation points with their associated hysteresis level crossings. The MS is moving from BS_0 to BS_1 and assumed to be communicating with BS_1 at the beginning of the interval shown, from [333]

To describe the signal strength based handoff algorithm, let

$$x(d) = \overline{\Omega}_{0\ (\mathrm{dB})}(d) - \overline{\Omega}_{1\ (\mathrm{dB})}(d) \tag{13.64}$$

denote the difference between the averaged signal strength estimates for BS_0 and BS_1. Consider the crossings of $x(d)$ with respect to the hysteresis levels $\pm H$ dB as illustrated in Fig. 13.14. A handoff is triggered if $x(d)$ has a down-crossing at $-H$ dB given that the last level crossing was an up-crossing at H dB, or if $x(d)$ has an up-crossing at H dB given that the last level crossing was a down-crossing at $-H$ dB. Vijayan and Holtzman verified that the two point processes, up-crossings of H dB and down-crossings of $-H$ dB, can be modeled as independent Poisson processes under the assumption that $x(d)$ is a stationary zero-mean Gaussian random process, i.e., changes in the mean are ignored and the MS is moving along the boundary between two cells [333]. This result also applies when $x(d)$ has non-zero mean, but in this case the up-crossing and down-crossing rates are not equal. The Poisson assumption is asymptotically true for large H, but has been shown to hold true for H values of practical interest, i.e., those on the order of the shadow standard deviation σ_Ω [333].

The handoff analysis proceeds by dividing up a handoff route into small spatial intervals of length d_s, such that only one level crossing is likely to occur within each interval. The probability of handoff at distance $d = nd_s$ is [333]

$$p_{ho}(n) = p_d(n)p_{lu}(n) + p_u(n)(1 - p_{lu}(n)), \tag{13.65}$$

where $p_u(n)$ and $p_d(n)$ are the probability of an up-crossing or down-crossing in the nth interval, and $p_{lu}(n)$ is the probability that the last event was an up-crossing. In other words, the MS was assigned to BS_0 at the beginning of the nth interval. This can happen in one of the two mutually exclusive ways: (1) there is an up-crossing but no down-crossing in the $(n-1)$th interval, and (2) there are no crossings in the $(n-1)$th interval, and the last event before the $(n-1)$th interval was an up-crossing. By assuming $p_{lu}(1) = 1$, the following recursive equation for $p_{lu}(n)$ can be derived as a function of $p_u(n-1)$, $p_d(n-1)$ and $p_{lu}(n-1)$ [333]:

$$p_{lu}(n) = p_u(n-1)(1 - p_d(n-1)) + (1 - p_u(n-1))(1 - p_d(n-1))p_{lu}(n-1). \tag{13.66}$$

As detailed in [333], the probabilities $p_d(n)$ and $p_u(n)$ are functions of the mean $\mu_x(d)$, variance $\sigma_x^2(d)$, and variance of the derivative $\sigma_{\dot{x}}^2(d)$ of $x(d)$. These in turn are functions of the statistics of $\Omega_{0\ (\mathrm{dB})}(d)$ and $\Omega_{1\ (\mathrm{dB})}(d)$, which depend on the path loss and shadowing. The statistics of $\Omega_{0\ (\mathrm{dB})}(d)$ and $\Omega_{1\ (\mathrm{dB})}(d)$ are first evaluated, and afterwards the appropriate expressions for $p_d(n)$ and $p_u(n)$ are derived.

As discussed in Chap. 3, co-channel interference can be assumed to add on a power basis [265, 296]. Hence, in the presence of N_I co-channel interferers the signals received from BS_0 and BS_1 are, respectively,

$$\Omega_{0\ (\mathrm{dB})}(d) = 10 \log_{10} \left\{ \sum_{k=0}^{N_I} \Omega_{0,k(\mathrm{dB})}(d) \right\} \tag{13.67}$$

$$\Omega_{1\ (\mathrm{dB})}(d) = 10\log_{10}\left\{\sum_{k=0}^{N_I}\Omega_{1,k(\mathrm{dB})}(d)\right\}, \tag{13.68}$$

where $\Omega_{0,0(\mathrm{dB})}(d)$ and $\Omega_{1,0(\mathrm{dB})}(d)$ are the power of the desired signals from BS_0 and BS_1, respectively, and $\Omega_{0,k(\mathrm{dB})}(d)$ and $\Omega_{1,k(\mathrm{dB})}(d)$, $k = 1, \ldots, N_I$ are the powers of the interfering co-channel signals received at the same BSs. Once again, the $\Omega_{0,k(\mathrm{dB})}(d)$ and $\Omega_{1,k(\mathrm{dB})}(d)$ are log-normally distributed. As discussed in Sect. 3.1, the sum of log-normal random variables can be approximated by another log-normal random variable and, hence, $\Omega_{0\ (\mathrm{dB})}(d)$ and $\Omega_{1\ (\mathrm{dB})}(d)$ remain Gaussian. Here, the approximations suggested by Fenton–Wilkinson [265, 296], and Schwartz & Yeh [296] are considered. As a further benefit, this will allow us to compare the usefulness of these two log-normal approximations for this application.

Following the notation established in Sect. 3.1, define $\hat{\Omega} = \xi\Omega_{(\mathrm{dB})}$, where $\xi = \ln(10)/10 = 0.23026$. If the N_I interferers for BS_0 have means $\mu_{\hat{\Omega}_{0,k}}(d)$ and variance $\sigma^2_{\hat{\Omega}}$, then the mean and variance of $\hat{\Omega}_0(d)$ using the Fenton–Wilkinson approach are

$$\mu_{\hat{\Omega}_0}(d) = \frac{\sigma^2_{\hat{\Omega}} - \sigma^2_{\hat{\Omega}_0}(d)}{2} + \ln\left(\sum_{k=0}^{N_I} \mathrm{e}^{\mu_{\hat{\Omega}_{0,k}}(d)}\right) \tag{13.69}$$

$$\sigma^2_{\hat{\Omega}_0}(d) = \ln\left((\mathrm{e}^{\sigma^2_{\hat{\Omega}}} - 1)\frac{\sum_{k=0}^{N_I}\mathrm{e}^{2\mu_{\hat{\Omega}_{0,k}}(d)}}{\left(\sum_{k=0}^{N_I}\mathrm{e}^{\mu_{\hat{\Omega}_{0,k}}(d)}\right)^2} + 1\right), \tag{13.70}$$

where the conversion of $\mu_{\hat{\Omega}_0}(d)$ and $\sigma^2_{\hat{\Omega}_0}(d)$ to units of decibels is $\mu_{\Omega_0}(d) = \xi^{-1}\mu_{\hat{\Omega}_0}(d)$, and $\sigma^2_{\Omega_0}(d) = \xi^{-2}\sigma^2_{\hat{\Omega}_0}(d)$, respectively. Schwartz & Yeh's approach is a recursive technique that combines only two log-normal variates at a time. For example, combining $\hat{\Omega}_{0,0}(d)$ and $\hat{\Omega}_{0,1}(d)$ gives the intermediate result

$$\mu_{\hat{\Omega}_0}(d) = \mu_{\hat{\Omega}_{0,0}}(d) + G_1 \tag{13.71}$$

$$\sigma^2_{\hat{\Omega}_0}(d) = \sigma^2_{\hat{\Omega}} - G_1^2 - 2\sigma^2_{\hat{\Omega}}G_3 + G_2, \tag{13.72}$$

where G_1, G_2, and G_3 are defined by (3.20), (3.23), and (3.24), respectively. The final values of $\mu_{\hat{\Omega}_0}(d)$ and $\sigma^2_{\hat{\Omega}_0}(d)$ are obtained by recursion.

By using either of the two log-normal approximations, the mean $\mu_x(d)$ can be determined. Since $x(d)$ is modeled as a Gaussian random process, the probabilities $p_d(n)$ and $p_u(n)$ can be computed by using the same procedure used to determine the envelope level crossing rates in Sect. 2.1.5. In particular,

$$\begin{aligned} p_u(n) &= d_s\int_0^\infty \dot{x}p(H,\dot{x})\mathrm{d}\dot{x} \\ p_d(n) &= d_s\int_{-\infty}^0 |\dot{x}|p(H,\dot{x})\mathrm{d}\dot{x}, \end{aligned} \tag{13.73}$$

where $p(H,\dot{x})$ is the joint density function of $x(kd_s)$ and its derivative $\dot{x}(kd_s)$. Since $x(kd_s)$ and $\dot{x}(kd_s)$ are independent Gaussian random variables,

$$p_u(kd_s) = \frac{d_s}{\sqrt{2\pi b_0}}\exp\left\{-\frac{(H-\mu_x(kd_s))^2}{2b_0}\right\}\left(\mu_{\dot{x}}(kd_s)Q\left(-\frac{\mu_{\dot{x}}(kd_s)}{\sqrt{b_2}}\right) + \sqrt{\frac{b_2}{2\pi}}\exp\left\{-\frac{-\mu^2_{\dot{x}}(kd_s)}{2b_2}\right\}\right), \tag{13.74}$$

where, from (2.102) with $f_q = 0$,

$$b_0 = \sigma_x^2(d) = 2\int_0^\infty \hat{S}_{xx}(f)\mathrm{d}f \tag{13.75}$$

$$b_2 = \sigma_{\dot{x}}^2(d) = 2(2\pi)^2\int_0^\infty f^2\hat{S}_{xx}(f)\mathrm{d}f, \tag{13.76}$$

and $\hat{S}_{xx}(f)$ in this case represents the power spectrum of $x(d)$ that includes the effect of co-channel interference. Likewise,

$$p_d(kd_s) = \frac{d_s}{\sqrt{2\pi b_0}} \exp\left\{-\frac{(H+\mu_x(kd_s))^2}{2b_0}\right\}\left(-\mu_{\dot{x}}(kd_s)Q\left(\frac{\mu_{\dot{x}}(kd_s)}{\sqrt{b_2}}\right)+\sqrt{\frac{b_2}{2\pi}}\exp\left\{-\frac{-\mu_{\dot{x}}^2(kd_s)}{2b_2}\right\}\right). \quad (13.77)$$

The autocorrelation of $\Omega_{0\ (\mathrm{dB})}(d)$ or $\Omega_{1\ (\mathrm{dB})}(d)$ (equal to the shadow autocorrelation) without co-channel interference is modeled by

$$\phi_{\Omega_{(\mathrm{dB})}\Omega_{(\mathrm{dB})}}(d) = \sigma_\Omega^2 \exp(-|d_1 - d_2|/d_0), \quad (13.78)$$

where $d = d_1 - d_2$, and d_0 controls the decorrelation with distance. Let $\tilde{\phi}_{\Omega_{(\mathrm{dB})}\Omega_{(\mathrm{dB})}}(d)$ denote the same autocorrelation function when co-channel interference is present. The value $\tilde{\phi}_{\Omega_{(\mathrm{dB})}\Omega_{(\mathrm{dB})}}(0)$ can be accurately approximated by using either (13.70) or (13.72). An approximation of $\tilde{\phi}_{\Omega_{(\mathrm{dB})}\Omega_{(\mathrm{dB})}}(d)$ for $d > 0$ can be obtained by substituting σ_Ω^2 in (13.78) with the value obtained in (13.70) or (13.72). The accuracy of this approximation was tested through the simulation of mutually uncorrelated log-normal interferers, each having the shadow autocorrelation in (13.78) with $\sigma_\Omega = 6$ dB and $d_0 = 20$ m. Figure 13.15 shows the results and verifies that the proposed approximation of $\tilde{\phi}_{\Omega_{(\mathrm{dB})}\Omega_{(\mathrm{dB})}}(d)$ is fairly accurate. Also, very accurate modeling of $\tilde{\phi}_{\Omega_{(\mathrm{dB})}\Omega_{(\mathrm{dB})}}(d)$ is not essential in handoff analysis [332].

Using the above approximation gives

$$\hat{S}_{xx}(f) = \frac{2(\sigma_{\Omega_0}^2(d) + \sigma_{\Omega_1}^2(d))d_0}{(1 + d_0^2(2\pi f)^2)(1 + d_{\mathrm{av}}^2(2\pi f)^2)}, \quad (13.79)$$

where $\sigma_{\Omega_0}^2(d)$ and $\sigma_{\Omega_1}^2(d)$ are obtained using either (13.70) or (13.72). This leads to

$$\sigma_x^2(d) = \frac{(\sigma_{\Omega_0}^2(d) + \sigma_{\Omega_1}^2(d))d_0}{d_0 + d_{\mathrm{av}}} \quad (13.80)$$

$$\sigma_{\dot{x}}^2(d) = \frac{\sigma_x^2(d)}{d_{\mathrm{av}}\ d_0}. \quad (13.81)$$

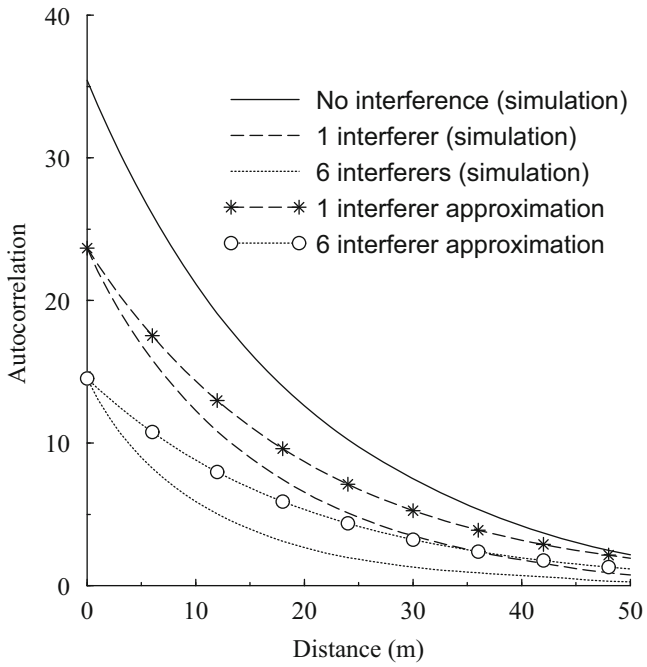

Fig. 13.15 Shadow autocorrelation with and without co-channel interference, from [25]

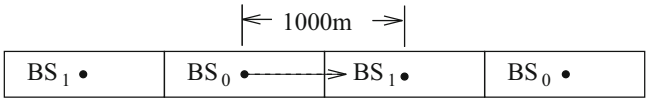

Fig. 13.16 Base station layout, MS route (*dotted line*), and location of co-channel interferers

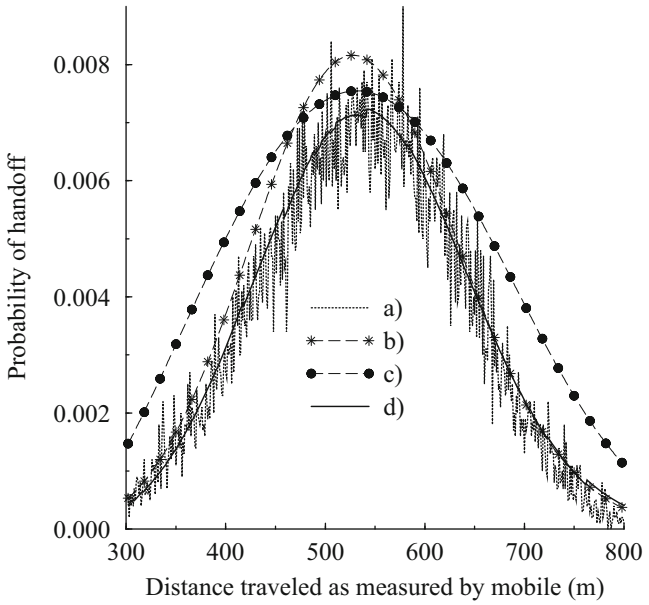

Fig. 13.17 Simulation vs. analytical model performance. a) Simulation of LoS handoff with co-channel interference, b) handoff analysis model in the absence of co-channel interference, c) handoff analysis model including co-channel interference and using the Fenton–Wilkinson log-normal approximation, d) handoff analysis model including co-channel interference and using the Schwartz & Yeh log-normal approximation, from [25]

13.6.1 Simulation Results

Consider a MS traversing from BS_0 to BS_1 separated by 1000 m with two co-channel interferers as shown in Fig. 13.16. Assume a square-law path loss with distance (used here to accentuate the co-channel interference effects), $d_{\text{av}} = 10\,\text{m}$, $d_0 = 20\,\text{m}$, and choose $\sigma_\Omega = 4\,\text{dB}$ so that both the Fenton–Wilkinson and Schwartz & Yeh log-normal approximations are accurate. Figure 13.17 compares analytical and simulation results for the handoff probabilities in the presence and absence of co-channel interference. Note that the presence of co-channel interference actually lowers the probability of handoff. Schwartz & Yeh's method leads to an accurate prediction of the handoff probabilities while the Fenton–Wilkinson method leads to less accuracy. Finally, the accuracy of the prediction of handoff probabilities leads us to conclude that the assumptions made for $\tilde{\phi}_{\Omega_{(\text{dB})}\Omega_{(\text{dB})}}(d)$ were reasonable.

13.7 CDMA Soft Handoff Analysis

In order to successfully deploy CDMA cellular systems it is essential to understand soft handoff behavior. As mentioned earlier, soft handoff has great impact on CDMA cellular system performance/capacity and studying its performance can provide crucial information on how the CDMA system performance can be optimized. Here, soft handoff in hierarchical CDMA architectures is considered. The treatment is divided into two main parts: interference analysis and handoff analysis. The first part of this section introduces an interference analysis, where the emphasis is on reverse link C/I performance and interference imbalance in hierarchical CDMA systems. When microcells are introduced to an existing macrocell layer the resulting interference imbalance between the layers can greatly impact the overall system performance. Therefore, it is important to characterize the interference in hierarchical CDMA architectures, and the interference analysis presented here provides a tool for studying the performance under soft handoff.

The second part of this section considers a soft handoff analysis method similar to that proposed in [10, 374], where a moving MS is tracked to determine its soft handoff active set membership. Such analysis is useful for determining cell boundaries and overall handoff efficiencies for a given set of handoff parameters. The studies in [10, 374] are limited to single MS and are not accurate when interference is taken into account. Here, soft handoff performance is considered in the presence of interference. This is accomplished by augmenting a user tracking soft handoff model with the results obtained from the interference analysis. The resulting model is useful for studying the impact of soft handoff parameters on soft handoff performance measures, such as handoff error probability and average active set membership. Finally, the effect of dynamic soft handoff parameter assignment is considered, where the soft handoff parameters are dynamically adjusted based on the given interference conditions. Dynamic parameter assignment offers a more efficient soft handoff mechanism than fixed assignment by reducing unnecessary soft handoff overhead.

13.7.1 System Model and Analysis

The channel model used here accounts for log-normal shadowing and path loss attenuation with distance.[4] The link gain between a MS located at (r, θ) and BS_i is

$$\begin{aligned} G_i(r,\theta) &= d_i(r,\theta)^{-\beta} 10^{\epsilon_i/10} \\ G_i(r,\theta)_{(\text{dB})} &= -\beta 10\log_{10}\{d_i(r,\theta)\} + \epsilon_i, \end{aligned} \tag{13.82}$$

where $d_i(r,\theta)$ is the distance between the MS and BS_i, β is the path loss exponent, and $10^{\epsilon_i/10}$ is the shadowing component such that ϵ_i has the normal distribution

$$\epsilon_i \sim \mathcal{N}(0, \sigma_\Omega^2), \tag{13.83}$$

where σ_Ω is the shadow standard deviation. Therefore, $G_i(r,\theta)$ also has log-normal distribution

$$G_i(r,\theta)_{(\text{dB})} \sim \mathcal{N}(\mu_i(r,\theta), \sigma_\Omega^2), \tag{13.84}$$

where

$$\mu_i(r,\theta) = -\beta 10\log_{10}\{d_i(r,\theta)\}. \tag{13.85}$$

Since our analysis involves a multi-cell system, the propagation model also accommodates shadow correlation between the multiple BS links:

$$\mathrm{E}[\epsilon_i \epsilon_j] = \rho\sigma_\Omega^2 \ , \quad i \neq j. \tag{13.86}$$

13.7.1.1 Interference Analysis

The system model used here for illustration consists of three macrocells and single microcell embedded within the macrocell layer as shown in Fig. 13.18, with the understanding that the methodology can readily be extended to larger deployments. The macrocells and microcell both use omnidirectional BS antennas. The microcell location is specified by the distance, d_μ, and angle, θ_μ, with respect to BS_1. Each macrocell area contains N MSs and the microcell area contains M MSs. The MSs are assumed to be uniformly distributed within each cell area. It is important to realize that the MSs located within a macro- or microcell area are not necessarily served by the BS located at the center of that macro- or micro-cell. Moreover, the model is not restricted to uniform macrocells either. Different MS densities within the macrocells can be realized by assigning different values of N to the macrocells and, likewise, by assigning different values of M to the microcells should there be more than one microcell. The introduction of the microcell in Fig. 13.18 will introduce interference imbalance into

[4] One can incorporate Rayleigh/Nakagami fading into our analysis by using a log-normal approximation for the composite log-normal Rayleigh/Nakagami distribution.

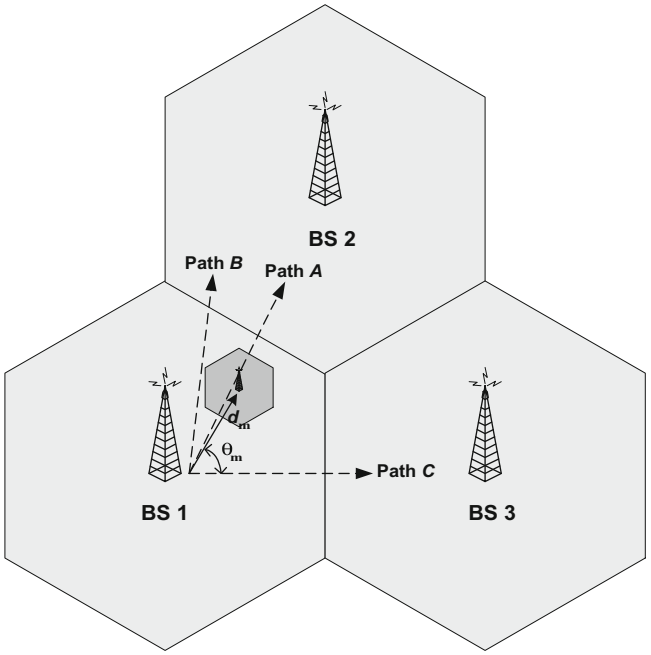

Fig. 13.18 Hierarchical CDMA system model

the overall system. Additional interference imbalance can be introduced by assigning different values of N to the macrocells as well. However, for exemplary purposes it is assumed that each macrocell area contains N uniformly distributed MSs.

Suppose that each MS connects to the BS that provides the least attenuation link. Given the location of a reference MS, r and θ in Cell 1, the probability that the MS is connected to BS_i is

$$\begin{aligned} \mathrm{P}_{\mathrm{H}1i}(r,\theta) &= \mathrm{P}[G_i(r,\theta) \geq G_j(r,\theta)\ ,\ \ j=1,2,3,\mu] \\ &= \int_{-\infty}^{\infty} \prod_{j\neq i} \Phi\left(\frac{\epsilon_i - \mu_j(r,\theta) - \rho[\epsilon_i - \mu_i(r,\theta)]}{\sqrt{(1-\rho^2)}\sigma_\Omega}\right) \frac{1}{\sqrt{2\pi}\sigma_\Omega} \exp\left\{-\frac{(\epsilon_i - \mu_i(r,\theta))^2}{2\sigma_\Omega^2}\right\} \mathrm{d}\epsilon_i. \end{aligned} \tag{13.87}$$

Therefore, the probability of the reference MS in Cell 1 being connected to BS_i is

$$\mathrm{P}_{\mathrm{H}1i} = \int_0^{2\pi} \int_0^{R_\mathrm{M}} \frac{r}{\pi R_\mathrm{M}^2} \mathrm{P}_{\mathrm{H}1i}(r,\theta)\mathrm{d}r\mathrm{d}\theta. \tag{13.88}$$

where R_M is the macrocell radius. Similarly, $\mathrm{P}_{\mathrm{H}2}$, $\mathrm{P}_{\mathrm{H}3}$, and $\mathrm{P}_{\mathrm{Hmicro}}$ can be calculated for the MSs located in different cells.

It may be argued that (13.87) is not representative of CDMA systems that employ power control and soft handoff. For these systems, a MS will connect to the BS that minimizes the transmit power required to achieve a target carrier-to-interference ratio (CIR). Looking at this another way, if a MS were to transmit with a given power P_T, it would connect to the BS that provides the largest carrier-to-interference ratio (CIR). Hence, under the assumption of ideal soft handoff, (13.87) becomes:

$$\begin{aligned} \mathrm{P}_{\mathrm{H}1i}(r,\theta) &= \mathrm{P}[\mathrm{CIR}_i(r,\theta) \geq \mathrm{CIR}_j(r,\theta)\ ,\ \ j=1,2,3,\mu] \\ &= \mathrm{P}\left[\frac{G_i(r,\theta)P_T}{I_i} \geq \frac{G_j(r,\theta)P_T}{I_j}\ ,\ \ j=1,2,3,\mu\right]. \end{aligned} \tag{13.89}$$

Later Sect. 13.7.2 shows that there is barely any difference between the two approaches in terms of handoff analysis. Moreover, handoff errors will be shown to sometimes occur where the MSs fail to connect to their ideal BSs. So an analysis based on ideal soft handoff is really an approximation as well. For these reasons, the analysis proceeds with the interference analysis based on (13.87). Later, this approach by extending the analysis to ideal soft handoff will be justified, using (13.89) instead of (13.87).

The total reverse link desired plus interfering signal power that is received by BS_i is equal to the sum of received power contributions from MSs located in different cells, i.e.,

$$S_i = S_i(1) + S_i(2) + S_i(3) + S_i(\mu), \tag{13.90}$$

where $S_i(j)$ is the signal contribution to BS_i from all MSs located in Cell j. With the introduction of a microcell, the level of interference that each BS experiences, I_i, will be uneven. Define γ_i as the interference power ratio between BS_i and the microcell:

$$\gamma_i \triangleq \frac{I_i}{I_\mu}. \tag{13.91}$$

Assuming a uniform CIR requirement and perfect power control, the signal power that is received from a MS connected to BS_i must satisfy

$$C_i = \gamma_i C_\mu, \tag{13.92}$$

where C_μ is the power controlled received power level of a MS connected to the microcell, which is used as a reference. Therefore,

$$I_i = S_i - C_i. \tag{13.93}$$

The power that is received at BS_i from MSs that are located in the Cell i cell, but are connected to BSs other than BS_i is now investigated. Let N_{ij} ($M_{\mu j}$) be the number of MSs in Cell i (Microcell) connected to BS_j:

$$\begin{aligned} N &= N_{i1} + N_{i2} + N_{i3} + N_{i\mu} \\ M &= M_{\mu 1} + M_{\mu 2} + M_{\mu 3} + M_{\mu\mu}. \end{aligned} \tag{13.94}$$

Define $\mathbf{N}_i$ as a vector containing the N_{ij}:

$$\mathbf{N}_i = (N_{i1}, N_{i2}, N_{i3}, N_{i\mu}). \tag{13.95}$$

Let us consider $S_1(1)$ as an example. Given $\mathbf{N}_1$,

$$S_1(1) = N_{11}C_1 + \sum_{k=1}^{N_{12}} S_{12}(1,k) + \sum_{k=1}^{N_{13}} S_{13}(1,k) + \sum_{k=1}^{N_{1\mu}} S_{1\mu}(1,k), \tag{13.96}$$

where $S_{ij}(q,k)$ is the interference contribution to BS_i from the kth MS located in Cell q and connected to BS_j. Under the assumption of perfect power control,

$$S_{ij}(q,k) = \frac{G_i(r,\theta)}{G_j(r,\theta)} C_j, \quad 0 < S_{ij}(q,k) < C_j. \tag{13.97}$$

The cumulative distribution function of $S_{ij}(q,k)$ for any MS, $S_{ij}(q)$, is then,

$$F_{S_{ij}(q)}(z) = \frac{1}{\mathrm{P}_{\mathrm{H}qj}} \int_0^{2\pi} \int_0^{R_\mathrm{M}} \frac{r}{\pi R_\mathrm{M}^2} \mathrm{P}\left[\frac{G_i(r,\theta)}{G_j(r,\theta)} C_j < z | \text{MS connected to } \mathrm{BS}_j\right] \mathrm{d}r\mathrm{d}\theta \tag{13.98}$$

Using the Gaussian distribution in (13.84) gives

$$F_{S_{ij}(q)}(z) = \frac{1}{\mathrm{P}_{\mathrm{H}qj}} \int_0^{2\pi} \int_0^{R_\mathrm{M}} \int_{-\infty}^{\infty} \frac{r}{\pi R_\mathrm{M}^2} \frac{1}{\sqrt{2\pi}\sigma_\Omega} \exp\left\{-\frac{(\varepsilon_j - \mu_j(r,\theta))^2}{2\sigma_\Omega^2}\right\}$$

$$\times\Phi\left(\frac{\varepsilon_j - 10\log_{10}[C_j/z] - \mu_i(r,\theta) - \rho[\varepsilon_j - \mu_j(r,\theta)]}{\sqrt{(1-\rho^2)}\sigma_s}\right)$$
$$\times\prod_{l\neq i,j}\Phi\left(\frac{\varepsilon_j - \mu_l(r,\theta) - \rho[\varepsilon_j - \mu_j(r,\theta)]}{\sqrt{(1-\rho^2)}\sigma_s}\right)\mathrm{d}r\mathrm{d}\theta\mathrm{d}\varepsilon_j. \tag{13.99}$$

Since $S_{ij}(q)$ is a nonnegative random variable, its expected value and the second moment are given as follows:

$$\begin{aligned}\mathrm{E}[S_{ij}(q)] &= \int_0^\infty (1 - F_{S_{ij}(q)}(z))\mathrm{d}z \\ &= \int_0^{C_j} (1 - F_{S_{ij}(q)}(z))\mathrm{d}z \\ \mathrm{E}[S_{ij}^2(q)] &= \int_0^{C_j} 2z(1 - F_{S_{ij}(q)}(z))\mathrm{d}z,\end{aligned} \tag{13.100}$$

and

$$\mathrm{Var}[S_{ij}(q)] = \mathrm{E}[S_{ij}^2(q)] - \mathrm{E}[S_{ij}(q)]^2. \tag{13.101}$$

Then, given $\mathbf{N}_1$, the mean and second moment of $S_1(1)$ are

$$\begin{aligned}\mathrm{E}[S_1(1)|\mathbf{N}_1] &= N_{11}C_1 + N_{12}\mathrm{E}[S_{12}(1)] + N_{13}\mathrm{E}[S_{13}(1)] + N_{1\mu}\mathrm{E}[S_{1\mu}(1)] \\ \mathrm{E}[S_1^2(1)|\mathbf{N}_1] &= N_{12}\mathrm{Var}[S_{12}(1)] + N_{13}\mathrm{Var}[S_{13}(1)] + N_{1\mu}\mathrm{Var}[S_{1\mu}(1)] \\ &\quad + N_{11}^2C_1^2 + N_{12}^2\mathrm{E}[S_{12}(1)]^2 + N_{13}^2\mathrm{E}[S_{13}(1)]^2 + N_{1\mu}^2\mathrm{E}[S_{1\mu}(1)]^2 \\ &\quad + \sum_{i=1} N_{1i}\mathrm{E}[S_{1i}(1)]\left(\sum_{j\neq i} N_{1j}\mathrm{E}[S_{1j}(1)]\right).\end{aligned} \tag{13.102}$$

The N_{1j} are binomial random variables with parameters $\mathrm{P}_{\mathrm{H}1j}$. Applying the chain rule of probability gives

$$\begin{aligned}\mathrm{E}[S_1(1)] &= \sum_{N_{11}=0}^{N}\binom{N}{N_{11}}\mathrm{P}_{\mathrm{H}11}^{N_{11}}(1-\mathrm{P}_{\mathrm{H}11})^{N-N_{11}} \\ &\quad\times\sum_{N_{12}=0}^{N-N_{11}}\binom{N-N_{11}}{N_{12}}\bar{\mathrm{P}}_{\mathrm{H}12}^{N_{12}}(1-\bar{\mathrm{P}}_{\mathrm{H}12})^{N-N_{11}-N_{12}} \\ &\quad\times\sum_{N_{13}=0}^{N-N_{11}-N_{12}}\binom{N-N_{11}-N_{12}}{N_{13}}\bar{\mathrm{P}}_{\mathrm{H}13}^{N_{13}}(1-\bar{\mathrm{P}}_{\mathrm{H}13})^{N-N_{11}-N_{12}-N_{13}}\mathrm{E}[S_1(1)|\mathbf{N}_1] \\ &= \sum_{N_{11}=0}^{N}\sum_{N_{12}=0}^{N-N_{11}}\sum_{N_{13}=0}^{N-N_{11}-N_{12}}\frac{N!}{N_{11}!N_{12}!N_{13}!N_{1\mu}!}\mathrm{P}_{\mathrm{H}11}^{N_{11}}(1-\mathrm{P}_{\mathrm{H}11})^{N-N_{11}} \\ &\quad\times\bar{\mathrm{P}}_{\mathrm{H}12}^{N_{12}}(1-\bar{\mathrm{P}}_{\mathrm{H}12})^{N-N_{11}-N_{12}}\bar{\mathrm{P}}_{\mathrm{H}13}^{N_{13}}(1-\bar{\mathrm{P}}_{\mathrm{H}13})^{N_{1\mu}}\mathrm{E}[S_1(1)|\mathbf{N}_1]\end{aligned} \tag{13.103}$$

$$\begin{aligned}\mathrm{E}[S_1^2(1)] &= \sum_{N_{11}=0}^{N}\sum_{N_{12}=0}^{N-N_{11}}\sum_{N_{13}=0}^{N-N_{11}-N_{12}}\frac{N!}{N_{11}!N_{12}!N_{13}!N_{1\mu}!}\mathrm{P}_{\mathrm{H}11}^{N_{11}}(1-\mathrm{P}_{\mathrm{H}11})^{N-N_{11}} \\ &\quad\times\bar{\mathrm{P}}_{\mathrm{H}12}^{N_{12}}(1-\bar{\mathrm{P}}_{\mathrm{H}12})^{N-N_{11}-N_{12}}\bar{\mathrm{P}}_{\mathrm{H}13}^{N_{13}}(1-\bar{\mathrm{P}}_{\mathrm{H}13})^{N_{1\mu}}\mathrm{E}[S_1^2(1)|\mathbf{N}_1]\end{aligned} \tag{13.104}$$

where

$$\bar{\mathrm{P}}_{\mathrm{H12}} = \frac{\mathrm{P}_{\mathrm{H12}}}{\mathrm{P}_{\mathrm{H12}} + \mathrm{P}_{\mathrm{H13}} + \mathrm{P}_{\mathrm{H1}\mu}} \tag{13.105}$$

$$\bar{\mathrm{P}}_{\mathrm{H13}} = \frac{\mathrm{P}_{\mathrm{H13}}}{\mathrm{P}_{\mathrm{H13}} + \mathrm{P}_{\mathrm{H1}\mu}}. \tag{13.106}$$

Finally, the variance of $S_1(1)$ is

$$\mathrm{Var}[S_1(1)] = \mathrm{E}[S_1^2(1)] - \mathrm{E}[S_1(1)]^2. \tag{13.107}$$

Similarly, the means and variances of $S_1(2)$, $S_1(3)$, and $S_1(\mu)$ can be obtained. Finally,

$$\begin{aligned}
\mathrm{E}[S_1] &= \mathrm{E}[S_1(1)] + \mathrm{E}[S_1(2)] + \mathrm{E}[S_1(3)] + \mathrm{E}[S_1(\mu)] \\
\mathrm{Var}[S_1] &= \mathrm{Var}[S_1(1)] + \mathrm{Var}[S_1(2)] + \mathrm{Var}[S_1(3)] + \mathrm{Var}[S_1(\mu)] \\
\mathrm{E}[I_1] &= \mathrm{E}[S_1] - C_1 \\
\mathrm{Var}[I_1] &= \mathrm{Var}[S_1].
\end{aligned} \tag{13.108}$$

Since I_1 represents a power sum, I_1 can be modeled as a log-normal random variable with the probability density function

$$p_{I_1}(x) = \frac{1}{x\sigma\sqrt{2\pi}} \exp\left\{ -\frac{(\ln(x) - \mu)^2}{2\sigma^2} \right\}, \tag{13.109}$$

where

$$\mathrm{E}[I_1] = \mathrm{e}^{\mu + \sigma^2/2} \tag{13.110}$$

$$\mathrm{Var}[I_1] = (\mathrm{e}^{\sigma^2} - 1)\mathrm{e}^{2\mu + \sigma^2}. \tag{13.111}$$

In a likewise fashion, the means and variances of I_2, I_3, and I_μ can be computed. The interference analysis can be run using the following iterative steps:

1. Set $C_1 = C_2 = C_3 = C_\mu$.
2. Compute means and variances of I_1, I_2, I_3, and I_μ.
3. Compute $\mathrm{E}[\gamma_i] = \mathrm{E}[I_i/I_\mu]$.
4. Set $C_i = \mathrm{E}[\gamma_i]C_\mu$.
5. Goto Step 2.

Usually, 15 iteration loops are sufficient for the γ_i to converge. Then the reverse link CIR becomes

$$(C/I)_i = C_i/I_i = C_\mu/I_\mu. \tag{13.112}$$

13.7.1.2 Soft Handoff Analysis

In CDMA cellular systems such as cdma2000 and WCDMA, each BS transmits a pilot signal, consisting of an unmodulated spreading sequence, to assist soft handoff. The MSs use the pilot signals to initiate and complete handoffs among other things. An *active set* refers to a set of BSs to which a MS is connected to at any given time. The active set contains multiple BSs when the MS is in soft handoff mode.

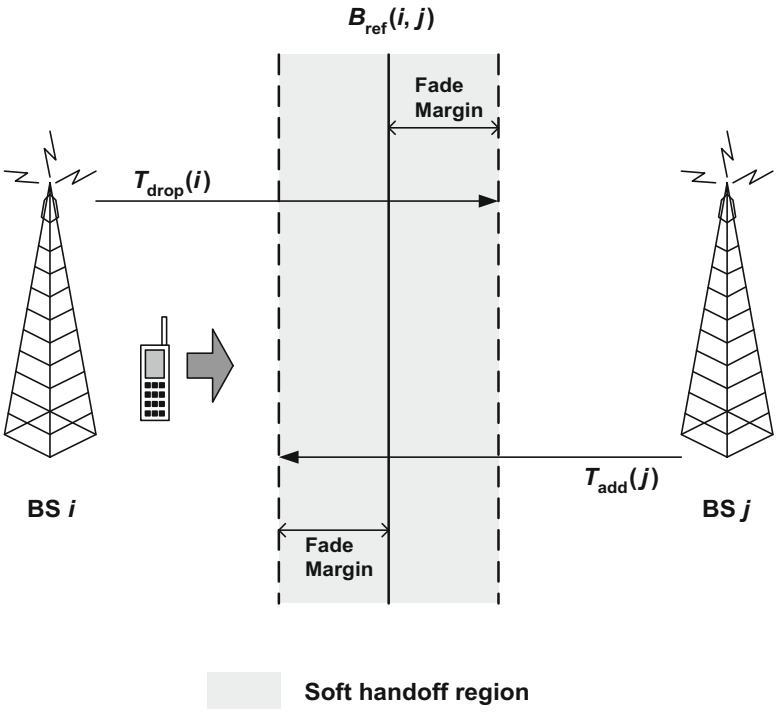

Fig. 13.19 Soft handoff parameters and corresponding handoff region

Suppose that the active set membership is based on the received pilot signal power.[5] The upper threshold, T_{add}, is the pilot signal level where qualifying BSs are added to the active set, whereas the lower threshold, T_{drop}, determines when the BSs are removed from the active set. The difference between T_{add} and T_{drop} is an indicator of how long a soft handoff will take on average. This is illustrated graphically in Fig. 13.19. Considering a MS that is traveling from BS_i to BS_j, the soft handoff region is determined by T_{drop} imposed on BS_i and T_{add} imposed on BS_j. The values of T_{add} and T_{drop} are determined by defining the reference boundary, B_{ref}, and adding a fade margin to combat the effect of shadow fading [336].

This section introduces a hierarchical soft handoff analysis similar to the analysis presented in [10, 374], which tracks a moving MS to observe its active set membership while incorporating the spatial correlation property of shadow fading. As mentioned previously, the introduction of microcell(s) into a macrocell layer results in interference imbalance which can impact the soft handoff decisions and performance. A handoff analysis based on received pilot signal strength and a single MS will not accurately depict the actual system behavior. On the other hand, a comprehensive analysis that includes multiple MSs while incorporating interference effects is prohibitively complicated and computationally exhaustive. Here, a soft handoff analysis model is presented that allows the study of soft handoff performance in conjunction with interference performance, by integrating the results obtained in interference analysis in Sect. 13.7.1.1. The approach accurately depicts the handoff performance of hierarchical systems, while being computationally efficient. Some detailed derivations are omitted in the following section, and refer the reader to [10, 374].

A MS traveling along a specific path is now considered to study its active set membership. Let $A(n)$ be the active set membership at epoch n for the MS under consideration. Let $\text{P}_i(n)$ be the probability that BS_i is in the active set at epoch n:

$$\text{P}_i(n) = \text{P}[\text{BS}_i \in A(n)]. \tag{13.113}$$

When $A(n)$ contains more than two BSs, the MS connects to the BS in the set that will minimize its transmit power, thereby limiting interference. This means that the BS selection within the set depends not only on the forward link received pilot strengths, but also the reverse link interference conditions. Let $B(n)$ be the BS in the active set that minimizes the MS transmit power. Since $A(n)$ is constantly being updated, the selection of $B(n)$ is based on the active set membership at epoch $n-1$:

[5] CDMA cellular systems actually use the forward link E_c/I_o, the ratio of the received pilot chip energy to total interference spectral density, to determine active set memberships. For the present purpose, the received pilot signal power is used instead and later in Sect. 13.7.2 the difference between these two methods for determining active set membership in terms of their soft handoff performance will be illustrated.

$$B(n) = \max\left\{ \frac{G_i(n)}{I_i(n)} \middle| \mathrm{BS}_i \in A(n-1) \right\}$$
$$= \max\left\{ \frac{G_i(n)}{\gamma_i(n)} \middle| \mathrm{BS}_i \in A(n-1) \right\}. \quad (13.114)$$

As mentioned before CDMA systems measure the forward link E_c/I_o to determine the active set memberships. However, for now just use the received pilot signal strength is used. It is also assumed that the BSs transmit their pilot signals with equal power. A BS is added to a MS's active set when its path gain exceeds its add threshold, $T_{\mathrm{add}}(i)$. Therefore, the probability that it will be added to the active set at epoch n is:

$$\mathrm{P}_{N\to i}(n) = \mathrm{P}[G_i(n) > T_{\mathrm{add}}(i) | \mathrm{BS}_i \notin A(n-1)]. \quad (13.115)$$

A BS is dropped from the active set by using both absolute and relative thresholds. First, the associated path gain must fall below the absolute drop threshold, $T_{\mathrm{drop}}(i)$. When it does, its gain is compared to the largest path gain in the active set, $B(n)$. When the difference between the two exceeds the relative drop threshold, $T_{\mathrm{rel}}(i)$, the BS is dropped from the active set. The relative threshold causes a BS to be dropped from the active set only when its link has deteriorated far below the best link. This also ensures that the active set contains at least one candidate BS at all times. The probability that BS_i is dropped from the active set at epoch n is:

$$\mathrm{P}_{i\to N}(n) = \mathrm{P}[B(n) - G_i(n) > T_{\mathrm{rel}}(i),\ G_i(n) < T_{\mathrm{drop}}(i) | \mathrm{BS}_i \in A(n-1)]. \quad (13.116)$$

Finally,

$$\mathrm{P}_i(n) = \mathrm{P}_i(n-1)[1 - \mathrm{P}_{i\to N}(n)] + [1 - \mathrm{P}_i(n-1)]\mathrm{P}_{N\to i}(n). \quad (13.117)$$

The main purpose of soft handoff is to ensure that the MS is connected to the BS which minimizes its transmit power. Therefore, a handoff error occurs when $B(n)$ is not the best available choice:

$$H_{\mathrm{error}}(n) = \mathrm{P}\left[B(n) \neq \max\left\{ \frac{G_1(n)}{I_1(n)}, \frac{G_2(n)}{I_2(n)}, \frac{G_3(n)}{I_3(n)}, \frac{G_\mu(n)}{I_\mu(n)} \right\} \right]$$
$$= \mathrm{P}\left[B(n) \neq \max\left\{ \frac{G_1(n)}{\gamma_1(n)}, \frac{G_2(n)}{\gamma_2(n)}, \frac{G_3(n)}{\gamma_3(n)}, G_\mu(n) \right\} \right]. \quad (13.118)$$

Another measure of soft handoff efficiency is the average number of BSs in active set at epoch n, $\bar{A}(n)$:

$$\bar{A}(n) = \mathrm{P}_1(n) + \mathrm{P}_2(n) + \mathrm{P}_3(n) + \mathrm{P}_\mu(n). \quad (13.119)$$

A smaller value of $\bar{A}(n)$ implies a lower infrastructure overhead to support soft handoff.

13.7.2 Numerical Results

A path loss exponent $\beta = 4$ and shadow standard deviation $\sigma_\Omega = 8$ dB are used in the simulation. Log-normal shadows are generated using the approach suggested in Sect. 2.6.1, where the parameter ζ_D is the spatial shadow correlation between two points separated by distance D m. The radii of the macrocell and microcell regions are set to 1500 and 100 m, respectively. Other important simulation parameters include:

- $\zeta_{100} = 0.82$
- $\rho = 0$ (uncorrelated shadowing)
- MS velocity = 60 km/h
- sampling period = 1 s
- $T_{\mathrm{rel}} = 3$ dB.

Table 13.2 Comparison of analytical and numerical results. Microcell load (M) is fixed at 12 while macrocell load (N) is varied

		Simulation				Analysis			
N	M	E[CIR] (dB)	E[γ_1]	E[γ_2]	E[γ_3]	E[CIR] (dB)	E[γ_1]	E[γ_2]	E[γ_3]
12	12	−12.70	0.135	0.096	0.093	−12.70	0.136	0.096	0.090
13	12	−12.86	0.148	0.110	0.107	−12.86	0.148	0.108	0.102
14	12	−13.03	0.162	0.128	0.125	−13.01	0.160	0.120	0.115
15	12	−13.19	0.176	0.145	0.142	−13.16	0.171	0.134	0.129
16	12	−13.34	0.188	0.163	0.162	−13.30	0.183	0.149	0.143
17	12	−13.50	0.203	0.181	0.182	−13.44	0.195	0.164	0.159
18	12	−13.64	0.219	0.204	0.208	−13.58	0.207	0.180	0.177
19	12	−13.79	0.232	0.225	0.229	−13.72	0.219	0.198	0.195

Table 13.3 Comparison of analytical and numerical results. Macrocell load (N) is fixed at 12 while microcell load (M) is varied

		Simulation				Analysis			
N	M	E[CIR] (dB)	E[γ_1]	E[γ_2]	E[γ_3]	E[CIR] (dB)	E[γ_1]	E[γ_2]	E[γ_3]
12	10	−12.25 dB	0.164	0.141	0.138	−12.23 dB	0.164	0.126	0.120
12	11	−12.48 dB	0.146	0.113	0.111	−12.47 dB	0.146	0.109	0.103
12	12	−12.70 dB	0.135	0.096	0.093	−12.70 dB	0.136	0.096	0.090
12	13	−12.92 dB	0.122	0.084	0.080	−12.92 dB	0.126	0.085	0.079
12	14	−13.13 dB	0.117	0.074	0.070	−13.13 dB	0.117	0.077	0.071
12	15	−13.34 dB	0.105	0.067	0.063	−13.33 dB	0.109	0.070	0.065
12	16	−13.53 dB	0.100	0.062	0.058	−13.52 dB	0.102	0.064	0.059
12	17	−13.72 dB	0.093	0.057	0.053	−13.71 dB	0.096	0.059	0.054

13.7.2.1 Interference Results

Tables 13.2 and 13.3 show the average CIR and interference performance comparisons between the analytical and simulation results. The microcell is placed at $d_\mu = 600\,\text{m}$ and $\theta_\mu = \pi/3$. Table 13.2 contains the results for varying macrocell load, N, while Table 13.3 shows the results when the microcell load, M, is varied. It is observed that the analytical and simulation results are in very close agreement, for both E[CIR] and E[γ_i]. It is also seen that the accuracy of the analytical results improves as the interference discrepancy between the layers increases (smaller γ_i). As expected, increasing the system load (N and M) results in a decrease in system CIR performance, since it causes the overall interference to increase. Since the density of MSs in the microcell is higher than the density of MSs in the macrocell by nature, the microcell experiences a higher level of interference than the macrocells. The γ_i indicate the degree of interference imbalance between the hierarchical layers, and the obtained results agree with our basic intuition; a larger microcell load increases the interference imbalance (smaller γ_i) while a smaller macrocell load decreases the interference imbalance (larger γ_i).

Figures 13.20 and 13.21 show the effect of microcell location on the average CIR and interference performance. The results are obtained by varying d_μ while θ_μ is fixed at $\pi/3$. Again, the analytical results are in close agreement with the simulation results. Figure 13.20 shows that the average CIR performance varies insignificantly with changes in microcell location, although it seems to benefit somewhat from diversity gain when the microcell is located very close to a macrocell BS. Figure 13.21 shows how the γ_i are affected by different microcell locations. It is observed that the corresponding γ_i increases as the microcell moves closer to a macrocell BS. This is expected since the level of inter-layer interference between the microcell and macrocell increases as the microcell gets closer to a macrocell BS, which in turn causes the macrocell interference to increase. Observe from Fig. 13.21 that as d_μ increases γ_1 decreases while γ_2 and γ_3 increase.

13.7.2.2 Soft Handoff Results

The previous section has shown how various system loads and microcell locations can affect the interference levels in hierarchical CDMA cellular systems. The interference imbalance factors (γ_i) are important parameters for determining the soft handoff performance since, along with the received pilot signal strengths, they can be used to portray the system behavior during soft handoff and provide information on how to improve the handoff performance. A fixed parameter handoff

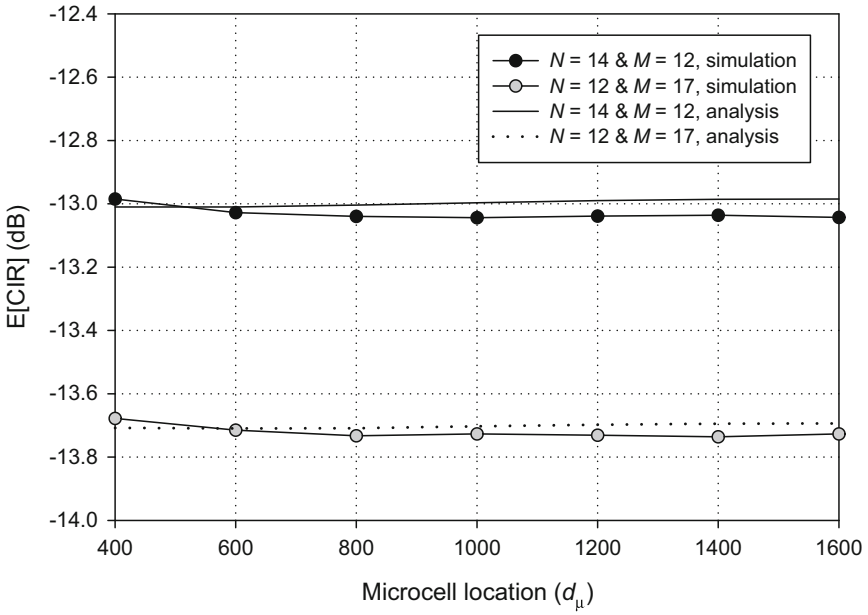

Fig. 13.20 Average CIR performance as a function of microcell location

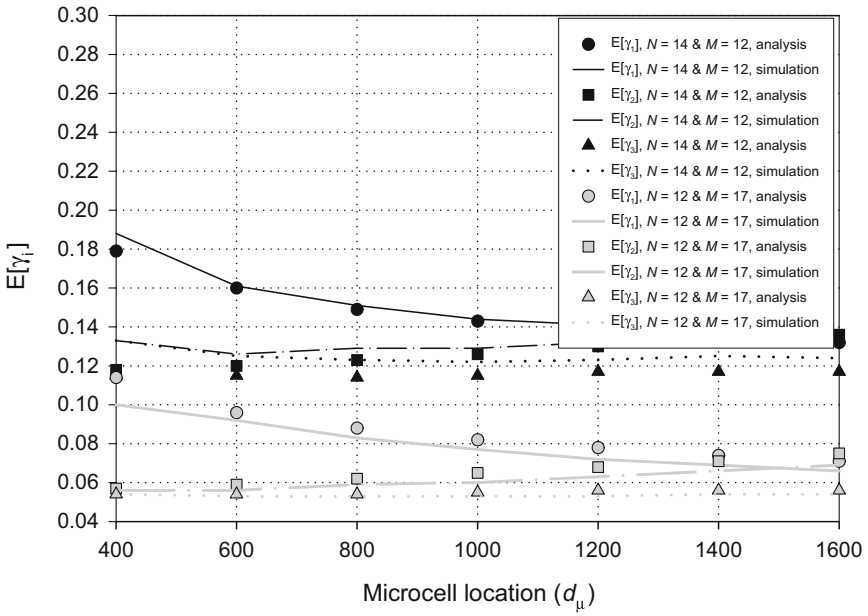

Fig. 13.21 $\mathrm{E}[\gamma_i]$ as a function of microcell location

algorithm is first considered, where the values of T_{add} and T_{drop} are fixed regardless of the changing interference conditions, and determined by defining B_{ref} at an equal distance location and assigning a fade margin of 8 dB,[6] viz.,:

$$\begin{aligned} T_{\text{add}}(i) &= B_{\text{ref}}(i,j) + 8 \text{ dB} \\ T_{\text{drop}}(j) &= B_{\text{ref}}(i,j) - 8 \text{ dB}. \end{aligned} \tag{13.120}$$

[6]Other fade margins can be chosen.

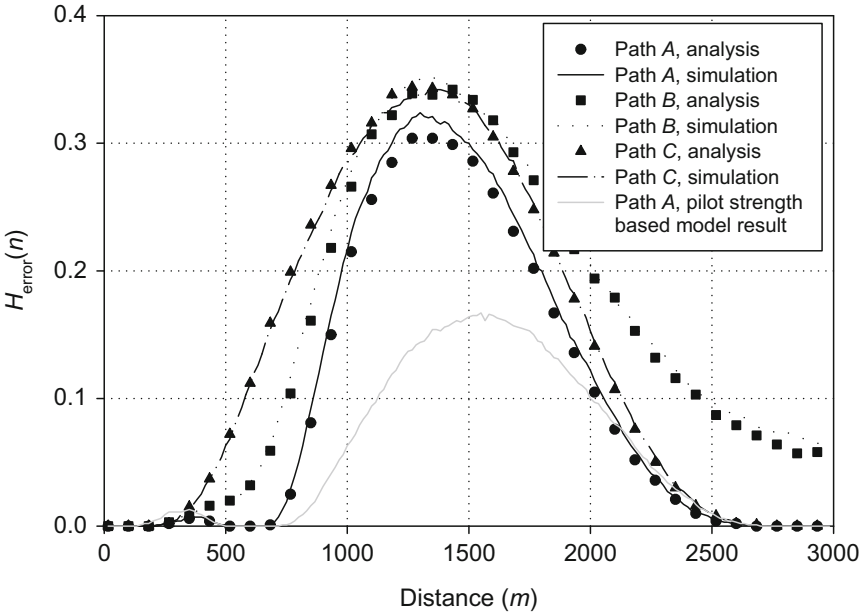

Fig. 13.22 Error performance of fixed handoff parameter assignment; $N = 13$ and $M = 12$

Figure 13.22 shows the handoff error probability for fixed handoff parameter assignment. The microcell is located at $d_\mu = 600$ m and $\theta_\mu = \pi/3$. The analytical results are obtained using $\mathrm{E}[\gamma_i]_{\text{analytical}}$ while the simulation results are obtained using actual γ_i. The figure shows the handoff error probability for three traveling paths, all starting from BS_1 as shown in Fig. 13.18. It is observed that the analytical and simulation results are in good agreement. Figure 13.22 also shows the handoff error probability for pilot-strength based handoff model [10, 374] and shows how it grossly underestimates the actual handoff error probability when interference levels are not uniform. By incorporating the interference analysis results, a far more accurate handoff performance analysis is obtained. The handoff error probability is observed to increase around the vicinity of physical cell boundaries. It is also observed that the handoff error probability is significantly higher between 1000 and 2000 m. This phenomenon is largely due to the value of σ_Ω and the selection of T_{drop} for BS_1 ($T_{\text{drop}}(1)$). $T_{\text{drop}}(1)$ has been set so that BS_1 is dropped from the active set once the MS enters the microcell. However, with $\sigma_\Omega = 8$ dB and with the effect of γ_1, BS_1 provides the best connection in the 1000–2000 m region a significant number of times, and that is why high values of $H_{\text{error}}(n)$ are observed. The handoff error probability can be improved by relaxing $T_{\text{drop}}(1)$ to cover the region, but this will definitely increase $\bar{A}(n)$, thereby leading to additional system resource requirements. However, the handoff error probability depends on the microcell location as shown in Fig. 13.23. The figure contains the handoff error probability plots for path A at three different microcell locations. It is seen that the handoff error probability decreases if d_μ is increased without changing $T_{\text{drop}}(1)$.

Next, the performance of dynamic handoff parameter assignment is examined. In dynamic parameter assignment B_{ref} is not fixed, but is dynamically updated as a function of the γ_i to improve the handoff performance. The concept is similar to the phenomenon of "cell breathing" [54, 319] where a heavily loaded cell shrinks in size and forces handoffs that will reduce interference. Our objective is to control the microcell handoff region according to given interference imbalance condition (as defined by the γ_i) to limit unnecessary overhead. This is accomplished by defining $B_{\text{ref}}(i, \mu)$ at the equilibrium point, d_e, where

$$\frac{d_e^{-\beta}(\mu)}{\gamma_i} = d_e^{-\beta}(i), \tag{13.121}$$

where $d_e(i)$ is the distance between d_e and BS_i. It is easily observed that $B_{\text{ref}}(i, \mu)$ moves toward the microcell BS as γ_i decreases which reduces the microcell soft handoff region accordingly. Figure 13.24 compares the performance between fixed and dynamic parameter assignment for path A with the microcell location at $d_\mu = 600$ m and $\theta_\mu = \pi/3$. While dynamic handoff parameter assignment does not offer any significant gain in handoff error probability, it provides a more efficient handoff mechanism over fixed handoff parameter assignment by reducing $\bar{A}(n)$. Fixed handoff parameter assignment requires a larger system overhead since it does not incorporate the system interference information into its handoff decisions.

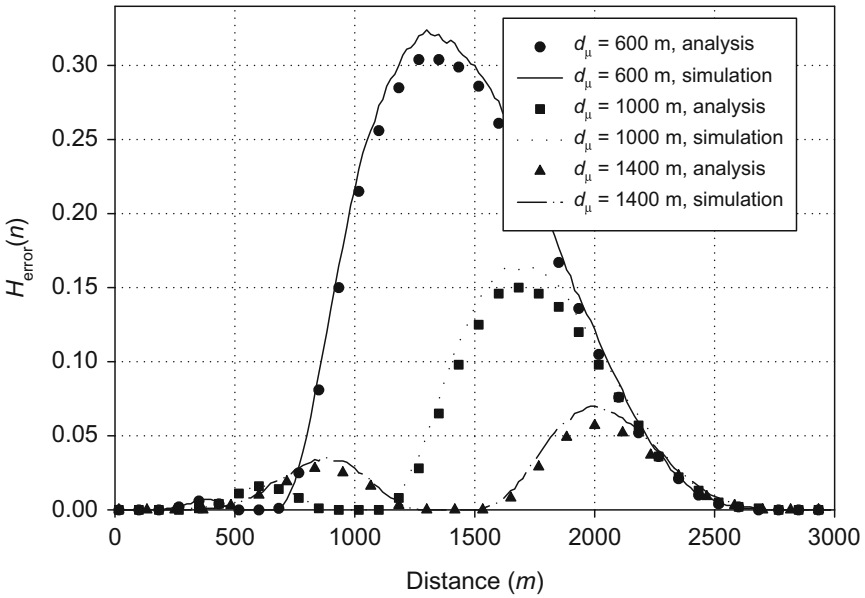

Fig. 13.23 Effect of microcell location on soft handoff performance; $N = 13$ and $M = 12$

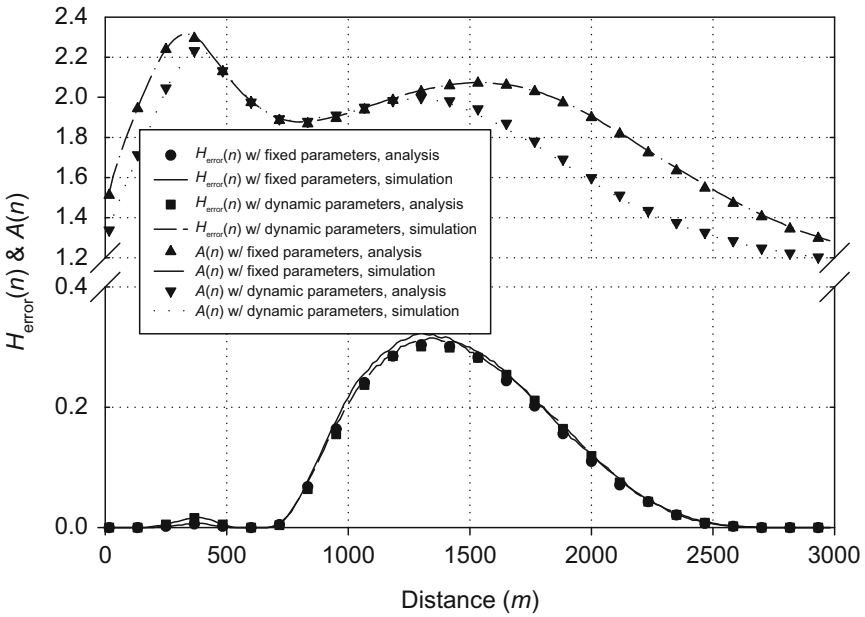

Fig. 13.24 Performance comparison between fixed and dynamic handoff parameter assignments; $N = 13$ and $M = 12$

Table 13.4 Comparison of fixed and dynamic soft handoff parameter assignment performances; $N = 13$ and $M = 12$

	Fixed		Dynamic	
Path	$E[H_{error}(n)]$	$E[\bar{A}(n)]$	$E[H_{error}(n)]$	$E[\bar{A}(n)]$
A	0.1043	1.8618	0.1033	1.7135
B	0.1598	1.7573	0.1584	1.6013
C	0.1406	1.8366	0.1314	1.6510

Dynamic handoff parameter assignment dynamically adjusts the microcell handoff region so that the system can prevent MSs from being prematurely subjected to soft handoff. Table 13.4 shows the average error probability and active set membership for three specified MS paths. For all three paths, dynamic handoff parameter assignment provides superior performance in $E[\bar{A}(n)]$ while slightly improving $E[H_{error}(n)]$.

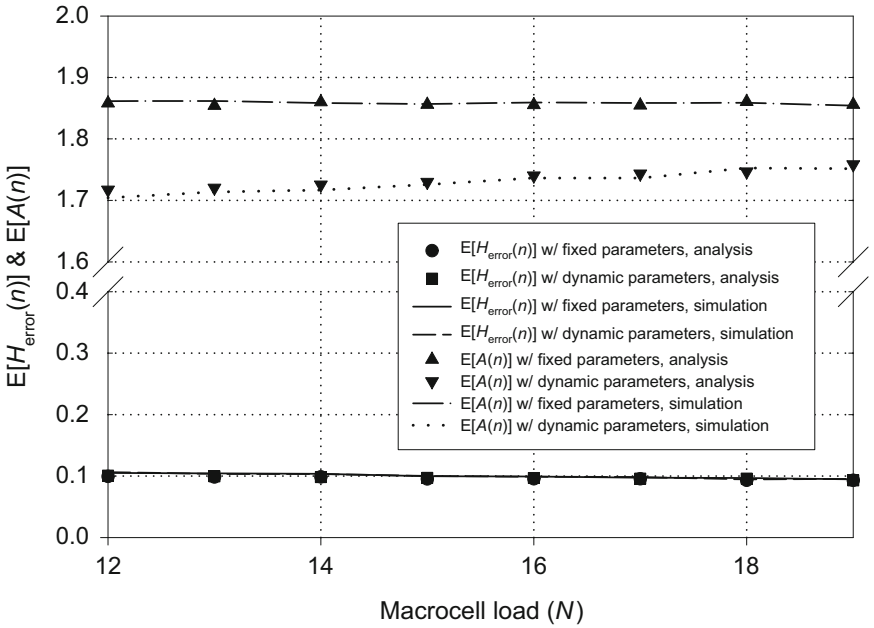

Fig. 13.25 Effect of interference imbalance on soft handoff performance. Microcell load (M) is fixed at 12 while macrocell load (N) is varied

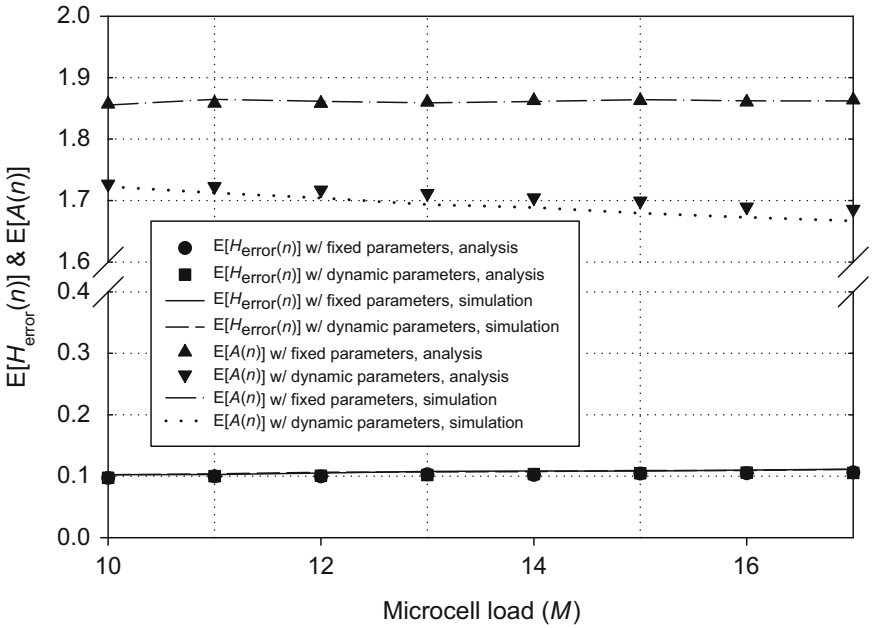

Fig. 13.26 Effect of interference imbalance on soft handoff performance. Macrocell load (N) is fixed at 12 while microcell load (M) is varied

Figures 13.25 and 13.26 compare the performance of fixed and dynamic handoff parameter assignment as the system load is varied. As was observed in Figs. 13.20 and 13.21, increasing the macrocell load, N, increases the γ_i while increasing the microcell load, M, reduces the γ_i. It is seen that $\mathrm{E}[\bar{A}(n)]$ stays nearly uniform with various system loads for fixed handoff parameter assignment while it changes according to the γ_i for dynamic handoff parameter assignment. As expected, a larger interference imbalance (lower γ_i) causes the microcell handoff region to shrink and thereby reducing $\mathrm{E}[\bar{A}(n)]$ for dynamic handoff parameter assignment. The average handoff error probabilities for both fixed and dynamic handoff parameter assignments do not change significantly with varying system load.

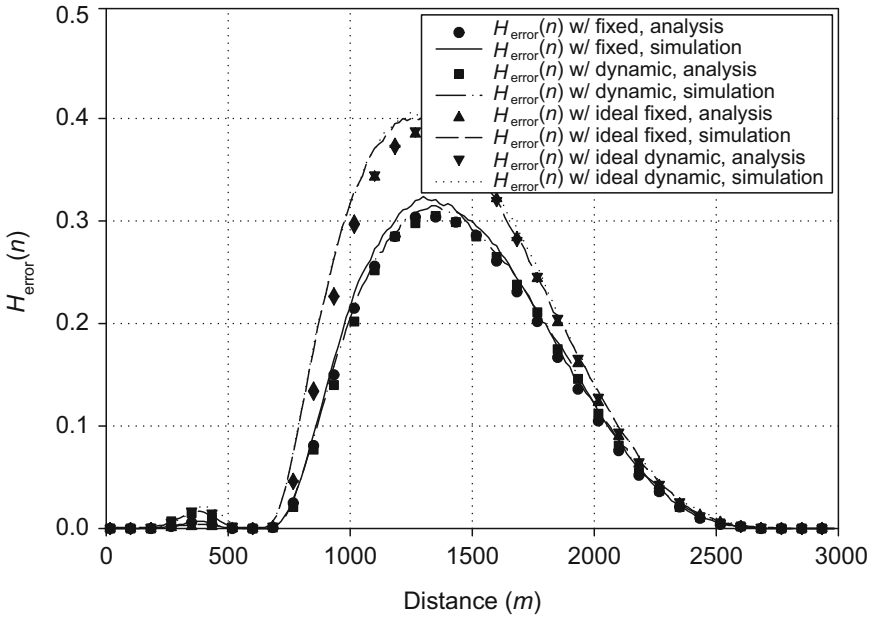

Fig. 13.27 Error performance comparison between our soft handoff assumption and ideal soft handoff; $N = 13$ and $M = 12$

13.7.2.3 Ideal Handoff and E_c/I_o-Based Active Set Membership

The soft analysis to this point has used some simplifying assumptions regarding soft handoff and its active set membership. The validity of these assumptions is now examined. In Sect. 13.7.1.1, it was assumed that a MS connects to the BS that provides the most robust path gain according to (13.87). However, during ideal soft handoff, a MS connects to the BS that minimizes its transmit power according to (13.89). Figures 13.27 and 13.28 compare the handoff error and the active set membership performance between the soft handoff analysis based on (13.87) and ideal soft handoff analysis based on (13.89). There is no significant performance difference between the two approaches. Also, dynamic handoff parameter assignment yields a more efficient handoff mechanism than fixed handoff parameter assignment in either case.

The analysis in Sect. 13.7.1.2 used the forward link received pilot signal power to determine active set membership, while practical CDMA systems use forward link E_c/I_o measurements instead. The difference between these two approaches is now examined. Let $P_T(i)$ be the total forward transmit power from BS i, including its pilot power. Then, for a MS located at (r, θ),

$$\frac{E_c(i)}{I_o(i)} \approx \frac{G_i(r,\theta)P_{\text{pilot}}}{\sum_{j=1}^{2,3,\mu} G_j(r,\theta)P_T(j)} G_{\text{spread}}, \tag{13.122}$$

where G_{spread} is the processing gain. There are two main difficulties when incorporating E_c/I_o into the soft handoff analysis. First, it is difficult to model the E_c/I_o behavior mathematically. A power controlled forward link is harder to model than its reverse link counterpart, especially with open loop power control. Second, the total forward transmit power from each BS, $P_T(i)$, depends on the number of MSs served by that BS including the MSs in soft handoff.

Once again the deployment in Fig. 13.18 introduces interference imbalance on the forward link due to the presence of the microcell. This interference imbalance will impact the received E_c/I_o from each BS. Figures 13.29 and 13.30 compare the pilot signal power and E_c/I_o methods for determining active set membership, in terms of the handoff error probability and average number of BSs in active set. These E_c/I_o based results are obtained by assuming that $P_T(i)$ is same for all BSs in the system, although this may not be true. There are some significant differences in performance between received pilot power and E_c/I_o based active set memberships. In particular, the E_c/I_o method requires much less overhead for a comparable handoff error performance. The observation may be attributed to the fact that E_c/I_o follows a slope up to $d^{-2\beta}$ and it has angular dependency. In either case, however, dynamic handoff parameter assignment yields a more efficient handoff mechanism than fixed handoff parameter assignment.

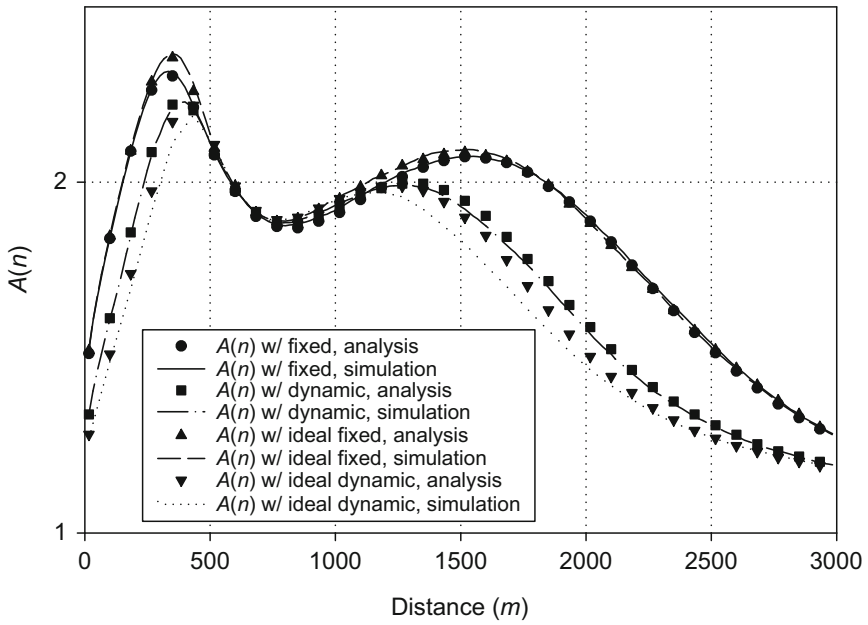

Fig. 13.28 Handoff overhead comparison between our soft handoff assumption and ideal soft handoff; $N = 13$ and $M = 12$

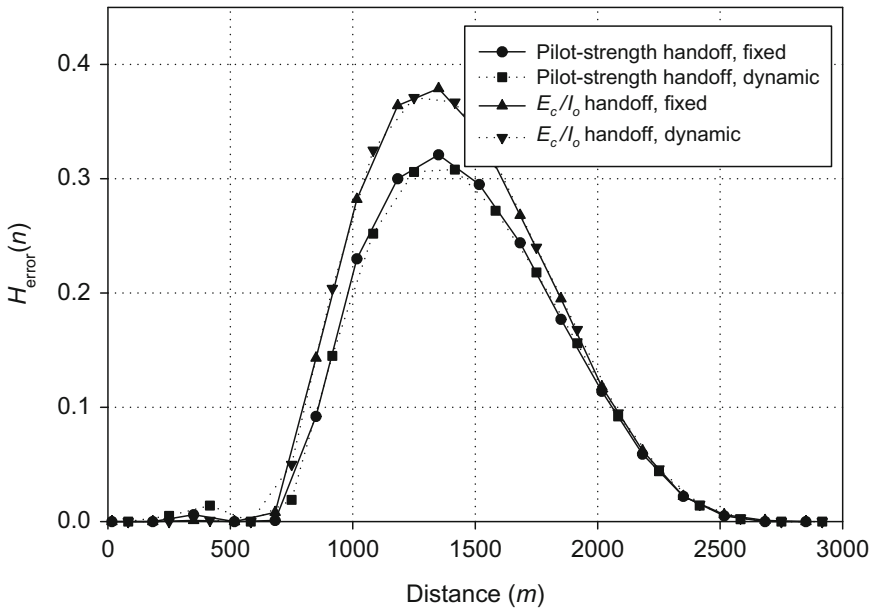

Fig. 13.29 Error performance comparison between pilot-strength and E_c/I_o based active set membership; $N = 13$ and $M = 12$

13.8 CINR Based Link Quality Measurements

Cellular radio resource allocation algorithms have been developed for handoffs [126], dynamic channel assignment [145, 241], and power control [20, 21], under the assumption that the MSs and/or BSs have access to real-time measurements of the received carrier-to-interference plus noise ratio $C/(I + N)$ or CINR. This section presents a technique for estimating $C + I + N$ and $C/(I + N)$ that could be used in resource management algorithms [29, 30].

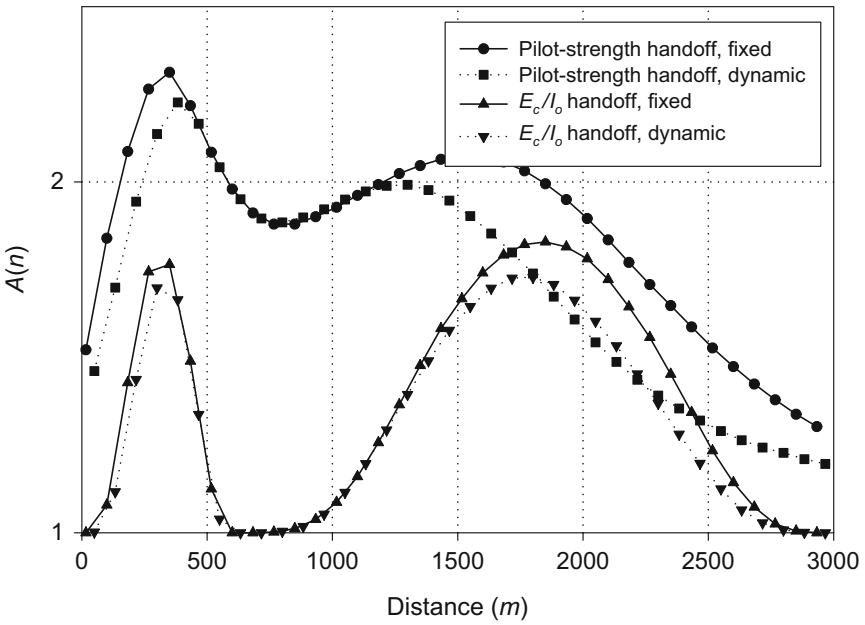

Fig. 13.30 Handoff overhead comparison between pilot-strength and E_c/I_o based active set membership; $N = 13$ and $M = 12$

13.8.1 Discrete-Time Model for Signal Quality Estimation

As shown in Sect. 7.2.1, the overall channel consisting of the transmit filter, waveform channel, matched filter, sampler, and noise whitening filter can be modeled as a T-spaced, $L + 1$-tap, transversal filter.[7] The overall discrete-time channel is described by the channel vector $\mathbf{g} = (g_0, g_1, \ldots, g_L)^T$, where $(\,)^T$ denotes transpose. Let $\mathbf{v} = (v_0, \ldots, v_M)^T$ denote the received signal vector consisting of M samples, where $v_k = \sum_{i=0}^{L} g_i x_{k-i} + w_k$. Assuming that the channel does not change significantly over a block of $L + M + 1$ symbols, the received vector $\mathbf{v}$ can be written as

$$\mathbf{v} = \mathbf{X}\mathbf{g} + \mathbf{w}, \tag{13.123}$$

where $\mathbf{X}$ is an $(M + 1) \times (L + 1)$ Toeplitz matrix consisting of the transmitted symbols of the form

$$\mathbf{X} = [x_{i,j}] = \begin{bmatrix} x_0 & x_{-1} & \cdots & x_{-L} \\ x_1 & x_0 & \cdots & x_{1-L} \\ \vdots & \vdots & \cdots & \vdots \\ x_M & x_{M-1} & \cdots & x_{M-L} \end{bmatrix} \tag{13.124}$$

and $\mathbf{w} = (w_0, \ldots, w_M)^T$ is an impairment vector consisting of the samples of the received interference plus AWGN.

13.8.1.1 Estimation of $I + N$

An $I + N$ or $C/(I + N)$ estimator requires a method for separating $\mathbf{g}$ and $\mathbf{w}$ from the observation of $\mathbf{v}$. Consider the situation where $M > L$, so that $\mathbf{X}$ has more rows than columns. Then, there exists a vector $\mathbf{c} = (c_0, \ldots, c_M)^T$ in the null space of $\mathbf{X}$ such that $\mathbf{c}^T\mathbf{X} = \mathbf{0}$. If $\mathbf{X}$ is known, then $\mathbf{c}$ can be easily determined. Then

$$\mathbf{c}^T\mathbf{v} = \mathbf{0} + \mathbf{c}^T\mathbf{w}, \tag{13.125}$$

[7] If rate $2/T$ sampling is used, then the overall channel is a $T/2$-spaced, $2L + 1$-tap, transversal filter.

and, therefore, $\mathbf{g}$ and $\mathbf{w}$ are completely separated from the observation $\mathbf{v}$. However, with the exception of training and pilot sequences, $\mathbf{X}$ is not known exactly because the data symbols comprising $\mathbf{X}$ must be obtained from symbol decisions. In such cases, a matrix of symbol decisions $\hat{\mathbf{X}}$ must be used instead, where $\hat{\mathbf{X}} = \mathbf{X} + \boldsymbol{\Delta}$ and $\boldsymbol{\Delta} = [\delta_{i,j}]$ is the symbol error matrix. Nevertheless, a vector $\hat{\mathbf{c}}$ can still be found in the null space of $\hat{\mathbf{X}}$ so that

$$\hat{\mathbf{c}}^T\mathbf{v} = \hat{\mathbf{c}}^T\mathbf{X}\mathbf{g} + \hat{\mathbf{c}}^T\mathbf{w}. \tag{13.126}$$

Hence, an (I+N) estimate can be obtained from

$$\begin{aligned}
\hat{\sigma}^2_{I+N} &= \frac{1}{2}\mathrm{E}\left[\frac{\mathbf{v}^H\hat{\mathbf{c}}^*\hat{\mathbf{c}}^T\mathbf{v}}{\|\hat{\mathbf{c}}\|^2}\right] \\
&= \frac{1}{2}\mathrm{E}\left[\frac{\mathbf{g}^H\boldsymbol{\Delta}^H\hat{\mathbf{c}}^*\hat{\mathbf{c}}^T\boldsymbol{\Delta}\mathbf{g}}{\|\hat{\mathbf{c}}\|^2}\right] + \frac{1}{2}\mathrm{E}\left[\frac{\mathbf{w}^H\hat{\mathbf{c}}^*\hat{\mathbf{c}}^T\mathbf{w}}{\|\hat{\mathbf{c}}\|^2}\right] \\
&= \frac{1}{2}\left(\sum_{i=0}^{L}\sum_{j=0}^{M}\sum_{k=0}^{L}\sum_{\ell=0}^{M}\mathrm{E}\left[\frac{\delta^*_{j,i}g^*_i\hat{c}^*_j\delta_{\ell,k}g_k\hat{c}_\ell}{\|\hat{\mathbf{c}}\|^2}\right] + \sum_{i=0}^{M}\sum_{j=0}^{M}\mathrm{E}\left[\frac{\hat{c}_i\hat{c}^*_j}{\|\hat{\mathbf{c}}\|^2}\right]\mathrm{E}[w_iw^*_j]\right),
\end{aligned} \tag{13.127}$$

where $(\,)^H$ denotes complex conjugate transpose, and where the second equality is obtained by using $\hat{\mathbf{X}} = \mathbf{X} + \boldsymbol{\Delta}$ along with the reasonable assumption that the impairment vector $\mathbf{w}$ has zero mean and is uncorrelated with $\mathbf{X}$ and $\mathbf{g}$. It is also reasonable to assume that the symbol errors are independent with a constant variance, i.e.,

$$\frac{1}{2}\mathrm{E}[|\delta_{j,i}|^2] = \sigma^2_\Delta. \tag{13.128}$$

It follows that

$$\hat{\sigma}^2_{I+N} = \Omega_p\sigma^2_\Delta + \frac{1}{2}\sum_{i=0}^{M}\sum_{j=0}^{M}\mathrm{E}\left[\frac{\hat{c}_i\hat{c}^*_j}{\|\hat{\mathbf{c}}\|^2}\right]\mathrm{E}[w_iw^*_j], \tag{13.129}$$

where $\Omega_p = \sum_{i=0}^{L}\Omega_i$ is the fading envelope power and $\Omega_i = \mathrm{E}[|g_i|^2]$ is the mean square value of the ith channel tap. To determine $\mathrm{E}[w_iw^*_j]$, rewrite the impairment vector $\mathbf{w}$ as

$$\mathbf{w} = \sum_{k=1}^{N_I}\mathbf{B}_k\mathbf{g}_k + \boldsymbol{\eta}, \tag{13.130}$$

where $\mathbf{B}_k$ is an $(M+1)\times(L+1)$ matrix consisting of the symbols from the kth interferer with associated channel tap vector $\mathbf{g}_k$, N_I is the number of interferers, and $\boldsymbol{\eta}$ is the vector of additive white Gaussian noise samples. The elements of $\mathbf{w}$ are

$$w_i = \sum_{k=1}^{N_I}\sum_{\ell=0}^{L}b_{k,i,\ell}\,g_{k,\ell} + \eta_i, \quad i = 0,\ldots,M, \tag{13.131}$$

where $\mathbf{B}_k = [b_{k,i,\ell}]$ and $\mathbf{g}_k = (g_{k,0},\ldots,g_{k,\ell})$. It is now assumed that the data symbols have zero mean, the data sequences comprising the $\mathbf{B}_k$ matrices for the interferers are both uncorrelated and mutually uncorrelated, and the η_i are independent zero-mean Gaussian random variables with variance σ^2_η. Then $\frac{1}{2}\mathrm{E}[w_iw^*_j] = 0$ for $i \neq j$ and

$$\begin{aligned}
\sigma^2_w = \frac{1}{2}\mathrm{E}[|w_i|^2] &= \frac{1}{2}\mathrm{E}\left[\sum_{k=1}^{N_I}\sum_{\ell=0}^{M}|b_{k,i,\ell}|^2\,|g_{k,\ell}|^2 + |\eta_i|^2\right] \\
&= \sum_{k=1}^{N_I}\sigma^2_b\sum_{\ell=0}^{L}\Omega_{k,\ell} + \sigma^2_\eta
\end{aligned}$$

$$= \sigma_I^2 + \sigma_\eta^2$$
$$= \sigma_{I+N}^2, \tag{13.132}$$

where $\sigma_b^2 = \frac{1}{2}\mathrm{E}[|b_{k,i,\ell}|^2]$ is the interferer symbol variance, $\Omega_{k,\ell} = \mathrm{E}[|g_{k,\ell}|^2]$ denotes the mean square value of the ℓth channel tap gain associated with the kth interferer, and σ_I^2 denotes the total interference power. Using this result, (13.129) becomes

$$\hat{\sigma}_{I+N}^2 = \Omega_p \sigma_\Delta^2 + \sigma_w^2 = \Omega_p \sigma_\Delta^2 + \sigma_{I+N}^2. \tag{13.133}$$

In practice, the ensemble averaging in the first line of (13.127) is replaced by an empirical average over P observation vectors $\mathbf{v}_i$ to provide the unbiased estimate

$$\hat{\sigma}_{I+N}^2 = \frac{1}{2P} \sum_{i=1}^{P} \frac{\mathbf{v}_i^H \hat{\mathbf{c}}_i^* \hat{\mathbf{c}}_i^T \mathbf{v}_i}{\|\hat{\mathbf{c}}_i\|^2}. \tag{13.134}$$

13.8.1.2 Estimation of $C/(I+N)$

A $C/(I+N)$ estimator can be formed by using $\hat{\sigma}_{I+N}^2$ as follows. The total received signal power from the desired signal, interfering signals, and noise is

$$\begin{aligned}
\sigma_{C+I+N}^2 &= \frac{1}{M+1}\frac{1}{2}\mathrm{E}\left[\mathbf{v}^H\mathbf{v}\right] \\
&= \frac{1}{M+1}\frac{1}{2}\mathrm{E}\left[\mathbf{g}^H\mathbf{X}^H\mathbf{X}\mathbf{g} + \mathbf{w}^H\mathbf{w}\right] \\
&= \frac{1}{M+1}\left(\sum_{j=0}^{L}\Omega_j \sum_{i=0}^{M}\frac{1}{2}\mathrm{E}[|x_{i,j}|^2] + (M+1)\sigma_w^2\right),
\end{aligned} \tag{13.135}$$

where the second equality follows from the assumption that $\mathbf{w}$ has zero mean, and the third equality requires that either the elements of the data sequence comprising the $\mathbf{X}$ matrix or the channel tap gains be uncorrelated. Now let $\sigma_X^2 = \frac{1}{2}\mathrm{E}[|x_{i,j}|^2]$. Then

$$\sigma_{C+I+N}^2 = \sigma_X^2 \Omega_p + \sigma_w^2 = \sigma_C^2 + \sigma_{I+N}^2. \tag{13.136}$$

Using (13.133) and assuming that σ_Δ^2 is sufficiently small such that $\Omega_p \sigma_\Delta^2 \approx 0$, the following $C/(I+N)$ estimate is obtained

$$\widehat{\mathrm{CIR}} = \left(\frac{\sigma_{C+I+N}^2}{\hat{\sigma}_{I+N}^2} - 1\right) \approx \frac{\sigma_C^2}{\sigma_{I+N}^2}. \tag{13.137}$$

The above approximation becomes exact when $\mathbf{X}$ is known exactly. This would be the case if $\mathbf{X}$ is formed by using elements from a known training sequence. Finally, by replacing ensemble averages with empirical averages, the following empirical $C/(I+N)$ estimate is obtained

$$\widehat{\mathrm{CIR}} = \frac{\frac{1}{M+1}\sum_{i=1}^{P}\mathbf{v}_i^H\mathbf{v}_i}{\sum_{i=1}^{P}\frac{\mathbf{v}_i^H\mathbf{c}_i^*\mathbf{c}_i^T\mathbf{v}_i}{\|\hat{\mathbf{c}}_i\|^2}} - 1. \tag{13.138}$$

13.8.2 Training Sequence Based $C/(I+N)$ Estimation

The bursts in TDMA cellular systems contain known training and/or color code sequences. The color code sequences are used for BS and sector identification, while the training sequences are used for synchronization and channel estimation. As can be seen from the previous section, the $I+N$ and $C/(I+N)$ estimators will only work well when σ_Δ^2 is small. Fortunately, if the $I+N$ and $C/(I+N)$ estimators are constructed from the training and color code sequences,[8] then $\sigma_\Delta^2 = 0$.

The $I+N$ and $C/(I+N)$ estimators of the previous section were evaluated through the software simulation for an IS-54/136 cellular system [104]. Although the IS-54/136 standard is now extinct, it is still serves as a useful example on how the $I+N$ and $C/(I+N)$ estimators can be applied. The IS-54 baud rate is 24,300 symbols/s and each frame is composed of 6 bursts of 162 symbols so that the frame rate is 25 frames/s. The MS is assumed to have correctly determined the serving BS, i.e., the color code is known, and is monitoring its half rate channel (one burst per frame). Therefore, the known symbols within a burst consist of the 14 symbol training sequence at the beginning of the burst, and a six symbol color code sequence in the middle of the burst as shown in Fig. 1.2. For simulation purposes, a two-equal-ray, T-spaced, Rayleigh fading channel was chosen with uncorrelated taps. If tap correlation is present, no changes are required to the proposed $I+N$ and $C/(I+N)$ estimators because the estimates depend only on the fading envelope power Ω_p. Shadowing is assumed to remain constant over the estimates and is neglected. Finally, it is assumed that the receiver has correctly synchronize onto each of the received bursts, i.e., perfect timing recovery is assumed.

Four consecutive symbols were used to form a 3×2 Toeplitz non-symmetric matrix $\mathbf{X}$. Let $\{v_1(i), \ldots, v_{14}(i)\}$ denote the 14 received samples corresponding to the training sequence and $\{v_{15}(i), \ldots, v_{21}(i)\}$ denote the six received samples corresponding to the color code of the ith frame. From the training sequence 4 estimates of $I+N$ and $C/(I+N)$ were formed by using the following four sets:

$$\{\{v_1(i), \ldots, v_4(i)\}, \{v_5(i), \ldots, v_8(i)\}, \{v_9(i), \ldots, v_{12}(i)\}, \{v_{11}(i), \ldots, v_{14}(i)\}\},$$

where the fourth set shares two samples with the third set. Likewise, 2 estimates of $I+N$ and $C/(I+N)$ were formed from the six symbol color code sequence by using the two sets

$$\{\{v_{15}(i), \ldots, v_{18}(i)\}, \{v_{17}(i), \ldots, v_{21}(i)\}\} \tag{13.139}$$

which share two common samples. Although the $I+N$ and $C/(I+N)$ estimators in (13.134) and (13.138) assume independent received sample vectors the additional estimates of $I+N$ and $C/(I+N)$ which use overlapped symbols at the ends of the training and color code sequences were found to improve the $I+N$ and $C/(I+N)$ estimates. The channel tap gains associated with the interferers were assumed to be constant during known symbol sequences. AWGN at 20 dB below the interference power was also included.

To evaluate the performance of the $I+N$ estimator, the average absolute percentage error between the $I+N$ estimate and the true interference plus noise power is defined as

$$\frac{\left|\hat{\sigma}_{I+N}^2 - \sigma_{I+N}^2\right|}{\sigma_{I+N}^2} \times 100. \tag{13.140}$$

Figure 13.31 depicts the average absolute percentage error over 500 independent averages for a specified averaging time (s), MS velocity (v), and number of interferers (N_I). Since the interference plus noise estimator is compared against σ_{I+N}^2 under the assumption that the fading has been averaged out, it is natural to expect the estimator to perform worse for lower MS velocities when the averaging length is short, as Fig. 13.31 illustrates. Nevertheless, the presence of multiple interferers can improve the estimate, since with multiple interferers it is less likely that the total interference power will be small due to fading.

Figure 13.32 depicts the average absolute percentage error between the $C+I+N$ estimate, $\hat{\sigma}_{C+I+N}^2$, and the true total received power, σ_{C+I+N}^2. As before, the MS velocity has a large effect on the estimator performance. Also, the C/I has a minor effect. However, in contrast to the $I+N$ estimator, the number of interferers has little effect for C/I between 5 and 20 dB and, hence, variations in the number of interferers are not shown in Fig. 13.32.

[8] In the IS-54 and PDC cellular systems, the color code sequence is known provided that the MS has correctly determined its serving BS.

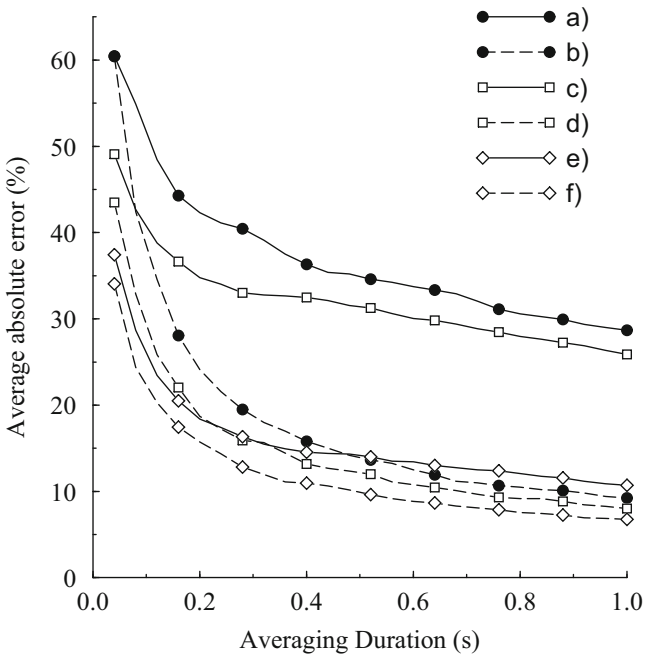

Fig. 13.31 Average absolute percent error of the $I+N$ estimator against the averaging time, from [30], [29]. The frame duration is 40 ms. Legend: a) $N_I = 1$, $v = 5$ km/h, b) $N_I = 1$, $v = 100$ km/h, c) $N_I = 2$, $v = 5$ km/h, d) $N_I = 2$, $v = 100$ km/h, e) $N_I = 6$, $v = 5$ km/h, f) $N_I = 6$, $v = 100$ km/h

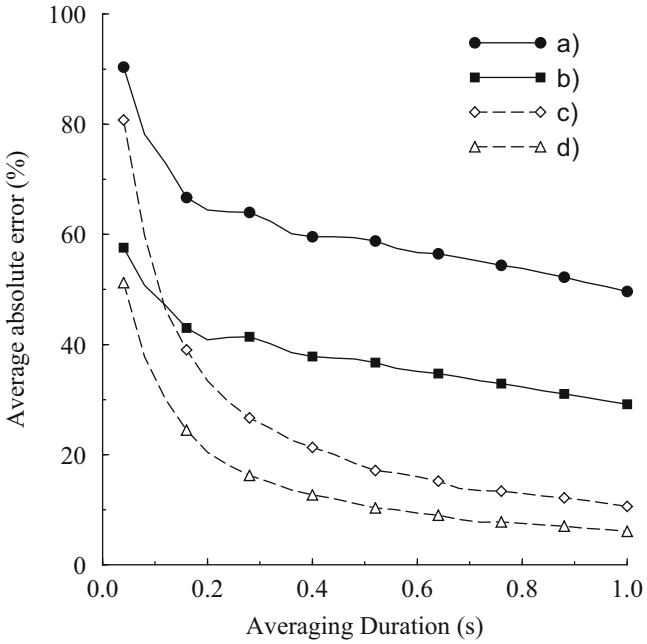

Fig. 13.32 Average absolute percent error of the $C+I+N$ estimator against the averaging time, from [29], [30]. The frame duration is 40 ms. Legend: a) $N_I = 1$, $v = 5$ km/h, $C/I = 5$ dB, b) $N_I = 1$, $v = 5$ km/h, $C/I = 20$ dB, c) $N_I = 1$, $v = 100$ km/h, $C/I = 5$ dB, d) $N_I = 1$, $v = 100$ km/h, $C/I = 20$ dB

Finally, Fig. 13.33 depicts performance of the $C/(I+N)$ estimator for an actual C/I of 5 dB. Only the performance with $C/I = 5$ dB is shown, since the estimator was found insensitive to C/I variations when the actual C/I was between 5 and 20 dB. For a high speed MS, the $C/(I+N)$ can be estimated to within 2 dB in less than a second. A slight improvement is also obtained when the MS uses two slots per frame (a full rate channel) as shown in Fig. 13.34.

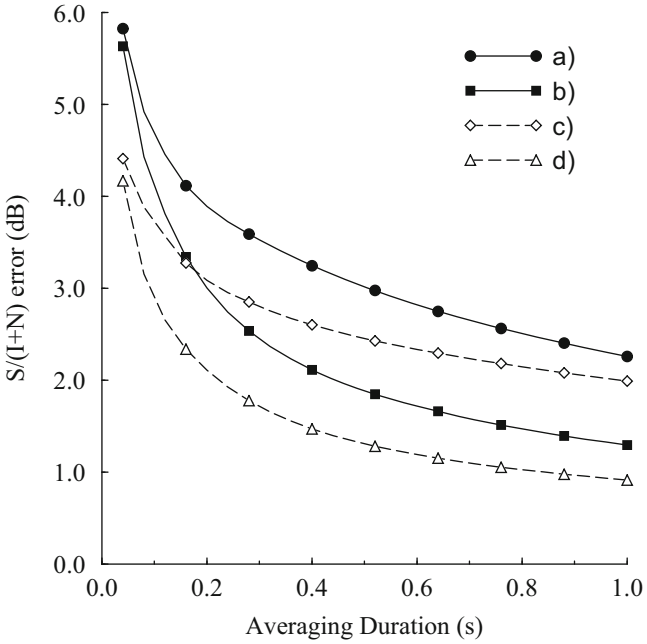

Fig. 13.33 Average error of the $C/(I+N)$ estimator against the averaging time, from [29], [30]. The frame duration is 40 ms. Legend: a) $N_I = 1$, $v = 5$ km/h, $C/I = 5$ dB, b) $N_I = 1$, $v = 100$ km/h, $C/I = 5$ dB, c) $N_I = 6$, $v = 5$ km/h, $C/I = 5$ dB, d) $N_I = 6$, $v = 100$ km/h, $C/I = 5$ dB

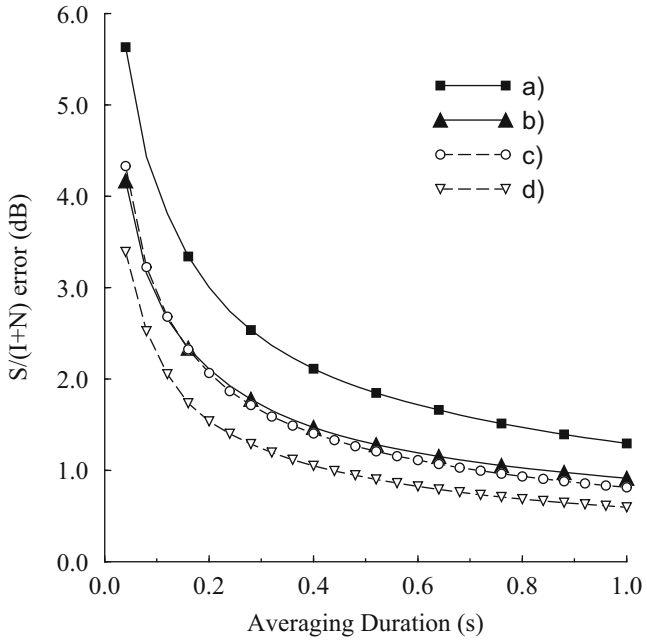

Fig. 13.34 Average error of the $C/(I+N)$ estimator for half rate and full rate channels against the averaging time, from [29], [30]. The frame duration is 40 ms. Legend: a) $N_I = 1$, $v = 100$ km/h, $C/I = 5$ dB, half rate channel, b) $N_I = 6$, $v = 100$ km/h, $C/I = 5$ dB, half rate channel, c) $N_I = 1$, $v = 100$ km/h, $C/I = 5$ dB, full rate channel, d) $N_I = 6$, $v = 100$ km/h, $C/I = 5$ dB, full rate channel

Appendix 13A: Derivation of Equations (13.43) and (13.58)

The limit in (13.58) can be written as

$$\lim_{\tau\to 0}\frac{\frac{\lambda_c}{2\pi\tau}\sqrt{\frac{2\tilde{\lambda}_{rr}(0)-2\tilde{\lambda}_{rr}(\tau)}{\tilde{\lambda}_{rr}(0)}}}{\frac{\lambda_c}{2\pi\tau}\sqrt{\frac{2\lambda_{rr}(0)-2\lambda_{rr}(\tau)}{\lambda_{rr}(0)}}}=\frac{\lim_{\tau\to 0}\frac{\lambda_c}{2\pi\tau}\sqrt{\frac{2\tilde{\lambda}_{rr}(0)-2\tilde{\lambda}_{rr}(\tau)}{\tilde{\lambda}_{rr}(0)}}}{\lim_{\tau\to 0}\frac{\lambda_c}{2\pi\tau}\sqrt{\frac{2\lambda_{rr}(0)-2\lambda_{rr}(\tau)}{\lambda_{rr}(0)}}}. \tag{13A.1}$$

Note that the limit of the denominator gives (13.43) and is a special case of the numerator limit with $N_o = 0$. To find the numerator limit, the following property can be used [309]:

If a function $f(\tau)$ has a limit as τ approaches a, then

$$\lim_{\tau\to a}\sqrt[n]{f(t)}=\sqrt[n]{\lim_{\tau\to a}f(t)} \tag{13A.2}$$

provided that either τ is an odd positive integer or n is an even positive integer and $\lim_{\tau\to a}f(\tau)>0$.

Therefore, if the limit

$$\zeta=\lim_{\tau\to 0}f^2(\tau)=\lim_{\tau\to 0}\frac{\lambda_c^2}{(2\pi\tau)^2}\frac{2\tilde{\lambda}_{rr}(0)-2\tilde{\lambda}_{rr}(\tau)}{\tilde{\lambda}_{rr}(0)} \tag{13A.3}$$

exists and is positive, the solution to (13A.1) can be determined. It is apparent that L'Hôpital's Rule should be applied to determine the limit in (13A.3). After substituting $\tilde{\lambda}_{rr}(\tau)$ from (13.34) and applying L'Hôpital's Rule four times, the limit is

$$\begin{aligned}\zeta=&\frac{{\lambda_c}^2\left(B_w^4{N_o}^2\pi^2+3B_wKN_o(2\pi f_m)^2b_0+2B_w^3KN_o\pi^2b_0+2B_w^3N_o\pi^2a(0)\right)}{6\pi^2\left(B_wN_o+2a(0)\right)\left(B_wN_o+4Kb_0+2a(0)\right)}\\&+\frac{{\lambda_c}^2\left(6K(2\pi f_m)^2b_0a(0)+3B_wKN_o(2\pi f_m)^2b_0\cos(2\theta_0)\right)}{6\pi^2\left(B_wN_o+2a(0)\right)\left(B_wN_o+4Kb_0+2a(0)\right)}\\&+\frac{{\lambda_c}^2\left(6K(2\pi f_m)^2b_0a(0)\cos(2\theta_0)\right)}{6\pi^2\left(B_wN_o+2a(0)\right)\left(B_wN_o+4Kb_0+2a(0)\right)}\\&+\frac{{\lambda_c}^2\left(-12a'(0)^2-12c'(0)^2-6B_wN_oa''(0)-12Kb_0a''(0)\right)}{6\pi^2\left(B_wN_o+2a(0)\right)\left(B_wN_o+4Kb_0+2a(0)\right)}\\&+\frac{{\lambda_c}^2\left(-12a(0)a''(0)-12c(0)c''(0)\right)}{6\pi^2\left(B_wN_o+2a(0)\right)\left(B_wN_o+4Kb_0+2a(0)\right)},\end{aligned} \tag{13A.4}$$

where $a(\tau)$ and $c(\tau)$ are given by (13.35) and (13.36), respectively, and $x'(0)$ denotes the derivative of $x(t)$ evaluated at $t = 0$. Consequently, $a(0) = b_0$, $a'(0) = c(0) = 0$, and

$$\begin{aligned}a''(0)&=b_0(2\pi f_m)^2\int_0^{2\pi}\hat{p}(\theta)\cos^2(\theta)\mathrm{d}\theta\\c'(0)&=b_02\pi f_m\int_0^{2\pi}\hat{p}(\theta)\cos(\theta)\mathrm{d}\theta.\end{aligned} \tag{13A.5}$$

Using these, and the identity $\cos^2(\theta) = (1 + \cos(2\theta))/2$, it can be shown that (13A.4) is positive for all θ for the scattering distributions considered in Sect. 13.4.3.1. Consequently, applying the theorem in (13A.2), the limit of the numerator of (13A.1) is the square root of (13A.4), which if desired can be expressed in terms of the signal-to-noise ratio γ_S using

$$b_0=\frac{\gamma_SN_oB_w}{2(K+1)} \tag{13A.6}$$

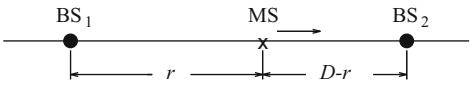

Fig. 13.35 MS traversing from BS_0 to BS_1 along a handoff route

from (13.53) with $K = s^2/2b_0$. The denominator of (13A.1), which is also (13.43), is obtained by assuming isotropic scattering and no noise, so that $a(0) = b_0$, $a'(0) = c(0) = c'(0) = c''(0) = 0$, $a''(0) = 2b_0(\pi f_m)^2$, and $N_o = 0$ in (13A.4). After taking the square root, the result is

$$\lim_{\tau \to 0} \frac{\lambda_c}{2\pi\tau} \sqrt{\frac{2\lambda_{rr}(0) - 2\lambda_{rr}(\tau)}{\lambda_{rr}(0)}} = v \sqrt{\frac{(1 + 2K + K\cos(2\theta_0))}{(1 + 2K)}}. \tag{13A.7}$$

Problems

13.1. Suppose that a MS is traveling along a straight line from BS_1 to BS_2, as shown in Fig. 13.35. The BSs are separated by distance D, and the MS is at distance r from BS_1 and distance $D - r$ from BS_2. Ignore the effects of fading and assume that the signals from the two BSs experience independent log-normal shadowing. The received signal power (in decibels) at the MS from each BS is given by (1.4).

- A handoff from BS_1 to BS_2, or vice versa, can never occur if $|\Omega_{1\ (\mathrm{dB})} - \Omega_{2\ (\mathrm{dB})}| < H$ but may or may not occur otherwise.
- A handoff from BS_1 to BS_2 will occur if the MS is currently assigned to BS_1 and $\Omega_{2\ (\mathrm{dB})} \geq \Omega_{1\ (\mathrm{dB})} + H$.

(a) Find an expression for the probability that a handoff can never occur from BS_1 to BS_2, or vice versa.
(b) Given that the MS is currently assigned to BS_1 what is the probability that a handoff will occur from BS_1 to BS_2.

13.2. A freeway with a speed limit of 120 km/h passes through a metropolitan area. If the average call duration is 120 s:

(a) What will be the average number of handoffs in a cellular system that uses omnidirectional cells having a 10 km radius.
(b) Repeat part (a) for a cellular system that uses 120° sectored cells having a 1 km radius.

13.3. A MS is moving with speed 100 km/h along a straight line between two base stations, BS_1 and BS_2. For simplicity ignore envelope fading and shadowing, and consider only the path loss. The received power (in dBm) follows the characteristic

$$\mu_{\Omega_{p\ (\mathrm{dBm})}}(d_i) = \mu_{\Omega_{p\ (\mathrm{dBm})}}(d_o) - 10\beta \log_{10}(d_i/d_o) \ \ (\mathrm{dBm}),$$

where d_i is distance from BS_i in meters. Assume $\mu_o = 0$ dBm at $d_o = 1$ m, and let the path loss exponent be $\beta = 3.0$.

Assume that the minimum usable signal quality at the receiver (at either link end) is $\mu_{\min} = -88$ dBm. The mobile station is connected to BS_1 and signal level at/from BS_1 is measured. The measured signal level is compared to a threshold μ_{HO}; if it drops below the threshold a handoff is initiated. Once the handoff is initiated it takes 0.5 s to complete.

(a) Determine the minimum margin $\Delta = \mu_{\mathrm{HO}} - \mu_{\min}$ so that calls are not lost due to weak signal strength during a handoff.
(b) What is the maximum allowable distance between BS_1 and BS_2?
(c) Describe the effects of the margin on the *link quality performance* and *capacity* of a cellular system.

13.4. Derive Eq. (13.19).

13.5. Derive Eq. (13.21).

13.6. Derive Eq. (13.34).

13.7. Derive Eq. (13.52).

13.8. Consider a communication link operating over a channel with propagation path loss exponent $\beta = 3.5$ and a shadow standard deviation $\sigma_\Omega = 8$ dB.

(a) Consider the case of two adjacent cells. A mobile station is transmitting at its maximum power and is located exactly on the cell boundary between the two base stations. In the absence of shadowing, the received power level would be equal to the receiver sensitivity, S_{RX}, i.e., the mobile station is located at distance d_{max} from each base station.

Now assume that shadowing *is* present and a soft handoff algorithm is used, such that the least attenuation link is always selected. The shadows experienced on the two possible links are independent. If an outage probability of 10% is desired for the given mobile station location (averaged over a large ensemble of realizations), what is the required margin $(M_{shad} - G_{HO})$, where M_{shad} is the required shadow margin for a single isolated cell and G_{HO} is the soft handoff gain?

(b) What is the value of G_{HO}?

(c) Repeat parts (a) and (b) assuming that the mobile is located on the boundaries of and equidistant from three base stations, i.e., the mobile station is located at distance d_{max} from three base stations.